Hindawi
Shock and Vibration
Volume 2020, Article ID 8819676, 26 pages
https://doi.org/10.1155/2020/8819676

Research Article

Dynamic Response of a Rotating Assembly under the Coupled Effects of Misalignment and Imbalance

Mohamed Desouki, Sadok Sassi, Jamil Renno, and Samer Abdelazim Gowid

Department of Mechanical and Industrial Engineering, College of Engineering, Qatar University, Doha, Qatar

Correspondence should be addressed to Sadok Sassi; sadok.sassi@qu.edu.qa

Received 9 May 2020; Revised 27 August 2020; Accepted 18 September 2020; Published 19 October 2020

Academic Editor: Paola Forte

In rotating machinery, the second most common fault after imbalance is misalignment. Misalignment can have a severe impact on equipment and may reduce the machine's lifetime considerably. In this paper, the simultaneous effect of imbalance and misalignment (parallel or angular) on the vibration spectra of rotating machinery will be discussed. A numerical model is developed and used to obtain the time and frequency responses of the rotor-coupling-bearing system to the simultaneous effect of these faults. The numerical model shows that the imbalance was mainly related to the peak located around 1X, whereas misalignment was linked to the peak around 2X. In addition, the parallel misalignment fault magnifies the 2X amplitude of the displacement response, whereas the response of angular misalignment is captured at the 2X and 4X amplitudes. This study also examines the effects of changing the model's rotational speed, misalignment level, and coupling type for angular and parallel misalignments.

1. Introduction

Rotating machinery is an essential part of many industrial sectors, and thus monitoring the condition of such machinery is continuously attracting researchers. The coupling is a vital part of any rotating machine, but it is often neglected because of its low cost against the total cost of the equipment. Flexible couplings are essential mechanical elements used in rotating machinery to allow power transmission between a driver and a driven shaft. Couplings are also used because they can compensate for inevitable misalignments between linked shafts. In the research literature, a strong focus on explaining the misalignment behavior in rotor dynamics has led to the experimental approach being used less frequently than numerical simulations. Suitable experimental methods include vibration analysis, torque, temperature capturing, and motor current consumption, whereas simulation methods include structural analysis, finite element (FE) analysis, and mathematical derivations. Out of all these methods used to capture misalignment faults, vibration spectrum analysis is the most widely accepted one. Here, we propose a numerical model that can evaluate the vibration response of misaligned shafts in rotating systems.

1.1. Misalignment in Rotating Shafts. Vibration in rotating machinery can sometimes be so dangerous that it destroys critical parts of the machine. The two primary sources of vibration within rotating mechanisms are rotor imbalance and shaft misalignment. Rotor imbalance is recognized as one of the most common origins of machine vibration, and it is present to some degree in nearly all rotating equipment. Physically, imbalance occurs when the center of mass (axis of inertia) of a rotating assembly does not coincide with the center of rotation (the geometric axis). Misalignment occurs when a rotating driveshaft, and the driven shafts coupled to it, does not rotate around the same central axis. Despite efforts to aligning interconnected shafts accurately, perfect alignment between shafts is challenging to maintain and achieve. Consequently, rotating machines often operate under less than optimum alignment conditions. This vexing

problem has challenged and intrigued maintenance professionals for decades because it can arise from many sources, including manufacturing and mounting tolerances, operational deflections caused by thermal expansion and distortion, foundation accommodation, working forces, and worn bearings [1]. The many different causes of misalignment are why this malfunction is known to be the second most frequent source of faults in rotating machinery, with only mass imbalance being more prevalent [2]. By itself, this problem represents more than 60% of failures reported in the industry [3, 4]. In the last decade, misalignment detection techniques have developed rapidly. However, there remains a need for a mechanism that describes misalignment phenomena more scientifically. There are many experimental methods for predicting misalignment faults, such as monitoring the motor's current, torque, acoustic, and vibration signals. The vibration-based diagnostics are most often used because vibration signals provide an abundance of mechanical information and are easier to collect [5]. Nevertheless, the vibration response of a system including a rotor, a coupling, and a bearing subjected to the coupled effects of misalignment and imbalance faults has not yet been fully explored.

1.2. Parallel and Angular Misalignments. In rotor dynamics, shafts have either parallel or angular misalignment, or both, as shown in Figure 1.

As portrayed in Figure 1, parallel misalignment is the condition when the axes of rotation are not collinear and do not intersect with each other. However, when the two axes of rotation are not collinear, but their centerlines intersect, this is known as angular misalignment. Parallel and angular misalignments can occur vertically and horizontally. Combined misalignment is the case where both parallel and angular misalignments exist simultaneously.

1.3. Experimental and Numerical Investigation of the Rotor-Coupling-Bearing System. In general, misalignment in the coupling leads to vibration throughout the mechanical system. The characteristic used to identify shaft misalignment includes a high level of axial vibrations, a 180° phase shift between axial vibrations on the shaft tips, and the manifest presence of a harmonic component in the signal spectrum at double the rotation speed; these are all widely accepted signs for fault diagnosis [6, 7], based on system vibrations. Sudhakar and Sekhar [8] reviewed the various methods that have been used for modeling the coupling, the effects of misalignment, and the condition monitoring techniques. Expressions for the forces and moments generated by parallel misalignment were defined by Gibbons [9]. Xu and Marangoni [10] explored misaligned rotor systems with imbalance and misalignment faults numerically and experimentally with flexible and helical couplings. Typically, peaks at the rotation speed (1X) and double the rotation speed (2X) were predominant in the vibration spectra. Sekhar and Prabhu [11] modeled the effects of coupling misalignment on rotor vibrations with eight degrees of freedom (DOFs) per node and developed expressions for the forces and moments involved in angular misalignment.

Despite the fact that 2X components on signal spectra are frequently reported as a sign of misalignment [12–14], varying results have been published, as shown in the theoretical work of Al-Hussain and Redmond [15], who showed that parallel misalignment manifests as synchronous vibrations. Moreover, the experimental results of different researchers revealed distinct spectral content for particular couplings under the same conditions of misalignment [3].

A simple linear mathematical model with flexible coupling was developed by Redmond [16] to analyze the forces in the system. He claimed that parallel misalignment by itself produces multiharmonic (i.e., 1X, 2X, and 3X) static and dynamic system responses. Lees [17], on the contrary, investigated rigid rotors and developed an analytical model for a linear system that included parallel misalignment but no damping. This linear model generated responses at multiple harmonics of the shaft's rotation speed. Jalan and Mohanty [18] used the residual generation method to develop a model-based fault detection method for a simple system involving a rotor and a bearing.

Similarly, Hariharan and Srinivasan [19, 20] developed an FE model of a simple rotor-bearing system with flexible coupling and correlated the FE model with experimental results for parallel misalignment only and found that in this case, 2X component was dominant. Xu and Marangoni [12] conducted experiments which showed that the vibration responses caused by misalignment occurred at even multiples of the rotational speed (2X, 4X, etc.). Patel et al. [21] developed a coupled rotor model that applied Timoshenko's beam theory as well as the effects of parallel and angular misalignments. Patel et al. used an experimental setup to discover diagnostic features in the 1X to 3X range. Sekhar and Prabhu [11] numerically estimated the effects of parallel misalignment on the vibration response at 2X within the rotating system. Jun-Lin and Yu-Chih Liu [22] used the concept of multiscale entropy alongside wavelet denoising to detect shaft misalignment. Dewell and Mitchell [13] showed experimentally that the vibration components at 2X and 4X mainly depend on misalignment in the coupling.

More recently, Hujare and Karnik [4] carried out experimental and numerical analysis (using FE models) for an aluminum shaft-rotor-bearing system with parallel misalignment. Misalignment effects at the coupling location were simulated via a nodal force vector. They observed that the impact of parallel misalignment was dominant at the characteristic 2X frequency rather than the 1X and 3X frequencies. The natural frequency has a crucial role in determining the speeds at which the characteristic 1X, 2X, and 3X frequencies reach their maximum amplitudes.

More recently, Li et al. [23] used an asymmetrical generator rotor system supported on journal bearings to examine the nonlinear dynamic behavior induced by parallel

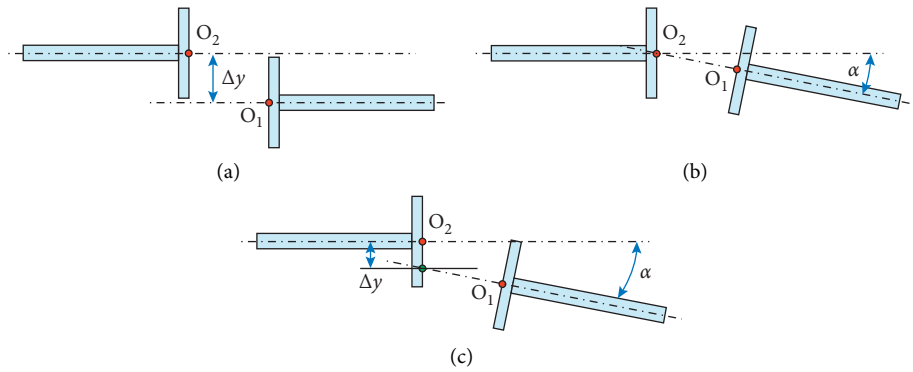

Figure 1: (a) Parallel misalignment, (b) angular misalignment, and (c) combined misalignment.

misalignment. By using numerical techniques (e.g., rotor orbits and their frequency spectra, Poincaré maps, and the greatest Lyapunov exponent), Li et al. [23] demonstrated that the supersynchronous component in the frequency spectrum at 2X was the key to identifying and diagnosing rotor misalignment.

Wand and Jiang [24] established a dynamic model for researching imbalance-misalignment coupling faults in a dual rotor system with intershaft bearing. Numerically and experimentally, they investigated the effect of the rotational speed ratio, mass eccentricity, misalignment angle, and parallel misalignment on the vibration characteristics of outer and inner rotors. The proposed model was verified by cascade plots, time waveforms, and frequency spectra. Recently, Wang and Gong [25] developed a comprehensive model to study misalignment and imbalance faults for a rotor system, of six degrees of freedom, via a FE approach. Misalignment effects were considered at the coupling location through the application of nodal force and moment vectors. Wang and Gong [25] managed to highlight some exciting features of parallel and angular misalignments in horizontal and vertical displacement forces and moments. Srinivas et al. [26] analyzed various system faults induced by angular misalignment within coupled rotor-train systems integrated with auxiliary active magnetic bearing (AMB) support. The method quantified the effect of misalignment by estimating additive coupling stiffness. The use of additive coupling stiffness to assess the severity of angular misalignment was a novel concept presented in this work. Sawalhi et al. [27] showed a detailed FE and dynamic simulation model of a vibration test rig. The result of the simulation was compared with experimental results. Both the simulated and experimental results showed an increase in the lower and higher harmonics of the shaft's rotational speed when the acceleration vibration signal with smearing was considered. Recently, the work presented in [28] investigated the deformation in a hexangular flexible coupling that joined a pair of rigid rotors that were misaligned (angular and parallel misalignments). The relationships among the vibration responses of the 1X, 2X, and 3X components and the moving orbits of the coupled rotors were simulated numerically at different speeds of rotation with and without misalignment. The results provided theoretical support for diagnosing and detecting faults within rotating machinery that includes hexangular flexible coupling.

The majority of the cited articles mainly focused on experimental and/or numerical investigations of angular and parallel misalignments. However, very few studies have analyzed a realistic case where misalignment and imbalance coexist simultaneously. Until now, these conditions have not been systematically investigated, although perfect balance in a rotating system is hard to achieve in practice, as some degrees of imbalance will always be present. Many of the previous studies had noticeable limitations since their systems were very complicated, or their theoretical developments were based on unrealistic assumptions that did not describe the combined effect of imbalance and misalignment, which were unable to capture real physical phenomena or were not applied in extreme cases of loading and deformation. Therefore, these systems are not easily available and/or often practically not applicable. Accordingly, this article aims to discuss the vibration features, nonlinear dynamics, and parameter properties of the combined effect of imbalance and misalignment in rotating machinery.

This paper is structured as follows: Section 2 presents the model used in this paper and provides a mathematical derivation of the forces and moments impacting the system as a result of misalignment and imbalance. Section 3 presents the results of various numerical experiments that were conducted and presents discussion of the results. Finally, Section 4 presents the conclusions of this research.

2. Modeling the Rotor-Coupling-Bearing System

2.1. Multibody Dynamic Model of the Rotating Assembly. The rotating assembly considered in the present investigation consists of two shafts connected together at their endpoints by a metallic spiral coupling. Each one of these

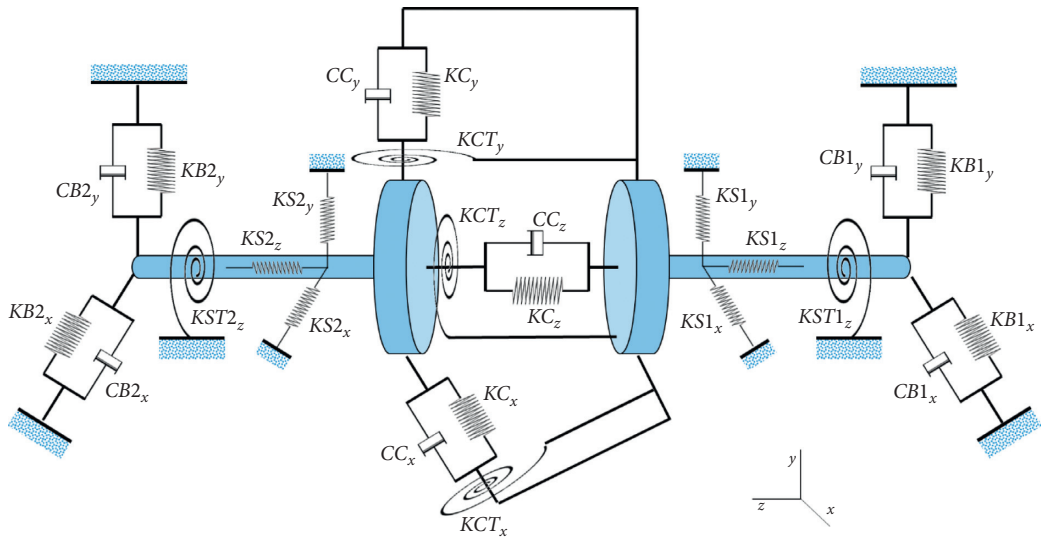

Figure 2: Multibody dynamic model of a rotating assembly (coupling + shafts + bearings).

shafts is partially supported, from the coupling side, by a ball bearing. To make the analysis nonspecific for a particular type of coupling and to ease comparisons with other investigations, the coupling was simulated as two disks, interconnected by stiffness and damping elements. A diagram of the assembly model, including the main components and geometric parameters, is presented in Figure 2.

The coordinate system was chosen in this model so that one of the axes (the z-axis) lay along the axial (longitudinal) direction of both shafts, whereas the x-axis and the y-axis lay along the radial directions. In the rest of the model description, the right-hand side of the coupling is indicated by the index 1, and the left-hand side is indicated by 2. Each of the coupling disks is able to move independently in three directions and to rotate freely around three axes. Therefore, with respect to Node 1, located at the center of gravity of the outer surface of disk 1, and to Node 2, located at the center of gravity of the outer surface of disk 2, the system's motion is described in total by 12 DOFs, in which each node has six DOFs, as indicated by the following equation:

$$q(t) = \left[x_1 \;\; x_2 \;\; y_1 \;\; y_2 \;\; z_1 \;\; z_2 \;\; \theta_1 \;\; \theta_2 \;\; \beta_1 \;\; \beta_2 \;\; \gamma_1 \;\; \gamma_2 \right]^T, \tag{1}$$

where x is the displacement in the radial horizontal direction, y is the displacement in the radial vertical direction, z is the displacement in the axial/longitudinal direction, θ is the rotation around the z-axis, β is the rotation around the x-axis, and γ is the rotation around the y-axis.

A second-order differential equation determines the motions of the rotor-coupling-bearing system shown in Figure 2:

$$[M]\{\ddot{q}\} + [C]\{\dot{q}\} + [K]\{q\} = \{F(t)\}, \tag{2}$$

where $[K]$ is the stiffness matrix, $[C]$ is the damping matrix, and $[M]$ is the mass matrix. Symbols with one dot and two dots in equation (2) represent the first and second derivatives with respect to time.

2.1.1. Determination of the Mass Matrix. The system's kinetic energy caused by rotation and translation motion is expressed as follows:

$$\begin{aligned} T = {} & \frac{1}{2}m_1\dot{x}_1^2 + \frac{1}{2}m_2\dot{x}_2^2 + \frac{1}{2}m_1\dot{y}_1^2 + \frac{1}{2}m_2\dot{y}_2^2 + \frac{1}{2}m_1\dot{z}_1^2 + \frac{1}{2}m_2 \\ & \cdot \dot{z}_2^2 + \frac{1}{2}I_{z1}\dot{\theta}_1^2 + \frac{1}{2}I_{z2}\dot{\theta}_2^2 + \frac{1}{2}I_{x1}\dot{\beta}_1^2 \\ & + \frac{1}{2}I_{x2}\dot{\beta}_2^2 + \frac{1}{2}I_{y1}\dot{\gamma}_1^2 + \frac{1}{2}I_{y2}\dot{\gamma}_2^2, \end{aligned} \tag{3}$$

where m_1 is the mass of Subsystem 1 (the right-hand side of the coupling), m_2 is the mass of Subsystem 2 (the left-hand side of the coupling), I_{x1} is the mass moment of inertia of Subsystem 1 in the x direction, I_{x2} is the mass moment of inertia of Subsystem 2 in the x direction, I_{y1} is the mass moment of inertia of Subsystem 1 in the y direction, I_{y2} is the mass moment of inertia of Subsystem 2 in the y direction, I_{z1} is the mass moment of inertia of Subsystem 1 in the z direction, and I_{z2} is the mass moment of inertia of Subsystem 2 in the z direction.

The coefficients of the mass matrix are obtained by the following derivative rule:

$$M_{ij} = \frac{\partial}{\partial \dot{q}_i}\frac{\partial}{\partial \dot{q}_j}(T). \tag{4}$$

By applying equation (4), we obtain the following expression of the mass matrix $[M]$:

$$\begin{bmatrix} m_1 & 0 & 0 & 0 & 0 & 0 & 0 & 0 & 0 & 0 & 0 & 0 \\ 0 & m_2 & 0 & 0 & 0 & 0 & 0 & 0 & 0 & 0 & 0 & 0 \\ 0 & 0 & m_1 & 0 & 0 & 0 & 0 & 0 & 0 & 0 & 0 & 0 \\ 0 & 0 & 0 & m_2 & 0 & 0 & 0 & 0 & 0 & 0 & 0 & 0 \\ 0 & 0 & 0 & 0 & m_1 & 0 & 0 & 0 & 0 & 0 & 0 & 0 \\ 0 & 0 & 0 & 0 & 0 & m_2 & 0 & 0 & 0 & 0 & 0 & 0 \\ 0 & 0 & 0 & 0 & 0 & 0 & lz_1 & 0 & 0 & 0 & 0 & 0 \\ 0 & 0 & 0 & 0 & 0 & 0 & 0 & lz_2 & 0 & 0 & 0 & 0 \\ 0 & 0 & 0 & 0 & 0 & 0 & 0 & 0 & lx_1 & 0 & 0 & 0 \\ 0 & 0 & 0 & 0 & 0 & 0 & 0 & 0 & 0 & lx_2 & 0 & 0 \\ 0 & 0 & 0 & 0 & 0 & 0 & 0 & 0 & 0 & 0 & ly_1 & 0 \\ 0 & 0 & 0 & 0 & 0 & 0 & 0 & 0 & 0 & 0 & 0 & ly_2 \end{bmatrix}. \tag{5}$$

2.1.2. Determination of the Stiffness Matrix. Based on the previously defined degrees of freedom, the equation for potential energy, in the shafts and coupling, is given by

$$\begin{aligned} V = {} & \frac{1}{2} KBS1_x x_1^2 + \frac{1}{2} KBS1_y y_1^2 + \frac{1}{2} KBS2_x x_2^2 + \frac{1}{2} KBS2_y y_2^2 \\ & + \frac{1}{2} KC_x (x_1 - x_2)^2 \\ & + \frac{1}{2} KC_y (y_1 - y_2)^2 + \frac{1}{2} KC_z (z_1 - z_2)^2 \\ & + \frac{1}{2} KCT_x (\beta_1 - \beta_2)^2 + \frac{1}{2} KCT_y (\gamma_1 - \gamma_2)^2 \\ & + \frac{1}{2} KCT_z (\theta_1 - \theta_2)^2 + \frac{1}{2} KS1_z z_1^2 + \frac{1}{2} KS2_z z_2^2 \\ & + \frac{1}{2} KS1T_z \theta_1^2 + \frac{1}{2} KS2T_z \theta_2^2, \end{aligned} \tag{6}$$

where the index B refers to the bearing, S refers to the shaft, C refers to the coupling, and T refers to torsion. In the previous expressions, since the two springs KB and KS are connected in parallel, their equivalent values will be

$$\begin{aligned} KBS1_x &= \frac{KB1_x}{KS1_x} = KB1_x + KS1_x, \\ KBS1_y &= \frac{KB1_y}{KS1_y} = KB1_y + KS1_y, \\ KBS2_x &= \frac{KB2_x}{KS2_x} = KB2_x + KS2_x, \\ KBS2_y &= \frac{KB2_y}{KS2_y} = KB2_y + KS2_y. \end{aligned} \tag{7}$$

Similarly, the coefficients of the stiffness matrix are obtained by the following derivative rule:

$$K_{ij} = \frac{\partial}{\partial q_i} \frac{\partial}{\partial q_j} (V). \tag{8}$$

Consequently, the stiffness matrix $[K]$ is given as

$$\begin{bmatrix} KBS1_x + KC_x & -KC_x & 0 & 0 & 0 & 0 & 0 & 0 & 0 & 0 & 0 & 0 \\ -KC_x & KBS2_x + KC_x & 0 & 0 & 0 & 0 & 0 & 0 & 0 & 0 & 0 & 0 \\ 0 & 0 & KBS1_y + KC_y & -KC_y & 0 & 0 & 0 & 0 & 0 & 0 & 0 & 0 \\ 0 & 0 & -KC_y & KBS2_y + KC_y & 0 & 0 & 0 & 0 & 0 & 0 & 0 & 0 \\ 0 & 0 & 0 & 0 & KC_z + KS1_z & -KC_z & 0 & 0 & 0 & 0 & 0 & 0 \\ 0 & 0 & 0 & 0 & -KC_z & KC_z + KS2_z & 0 & 0 & 0 & 0 & 0 & 0 \\ 0 & 0 & 0 & 0 & 0 & 0 & KCT_z + KS1T_z & -KCT_z & 0 & 0 & 0 & 0 \\ 0 & 0 & 0 & 0 & 0 & 0 & -KCT_z & KCT_z + KS2T_z & 0 & 0 & 0 & 0 \\ 0 & 0 & 0 & 0 & 0 & 0 & 0 & 0 & KCT_x & -KCT_x & 0 & 0 \\ 0 & 0 & 0 & 0 & 0 & 0 & 0 & 0 & -KCT_x & KCT_y & 0 & 0 \\ 0 & 0 & 0 & 0 & 0 & 0 & 0 & 0 & 0 & 0 & KCT_x & -KCT_y \\ 0 & 0 & 0 & 0 & 0 & 0 & 0 & 0 & 0 & 0 & -KCT_y & KCT_y \end{bmatrix}. \tag{9}$$

2.1.3. Determination of the Damping Matrix. There are numerous paths to damping, and in a complex structure, several means of damping may take place simultaneously at different locations throughout the structure. The damping considered in this work accounts for the interconnecting parts, at the endpoints of the shafts, namely, the bearings and the coupling, and the structural damping of the shafts themselves.

Viscous damping is a formulation of the damping phenomena, in which the force of damping is proportional to the velocity. Most often, viscous damping refers to dashpot, a simple technique used to model the energy dissipation in mechanical systems and thus represents several dissipative phenomena such as heat, friction, and plastic yielding. For those reasons, several dashpots were introduced in the system to account for viscous damping behavior. For the proposed model, the dissipation energy equation because of viscous damping is detailed as follows:

$$\begin{aligned} Dv = {} & \frac{1}{2}CB1_x\,\dot{x}_1^2 + \frac{1}{2}CB1_y\,\dot{y}_1^2 + \frac{1}{2}CB2_x\,\dot{x}_2^2 \\ & + \frac{1}{2}CB2_y\,\dot{y}_2^2 + \frac{1}{2}\,CC_x\,(\dot{x}_1 - \dot{x}_2)^2 \\ & + \frac{1}{2}\,CC_y(\dot{y}_1 - \dot{y}_2)^2 + \frac{1}{2}\,CC_z(\dot{z}_1 - \dot{z}_2)^2. \end{aligned} \tag{10}$$

The coefficients of the viscous damping matrix are obtained by using the following derivative rule:

$$Cv_{ij} = \frac{\partial}{\partial \dot{q}_i}\,\frac{\partial}{\partial \dot{q}_j}\,(Dv). \tag{11}$$

The produced viscous damping matrix $[C_v]$ is detailed below:

$$\begin{bmatrix} CB1_x + CC_x & -CC_x & 0 & 0 & 0 & 0 & 0\,0\,0\,0\,0\,0 \\ -CC_x & CB2_x + CC_x & 0 & 0 & 0 & 0 & 0\,0\,0\,0\,0\,0 \\ 0 & 0 & CB1_y + CC_y & -CC_y & 0 & 0 & 0\,0\,0\,0\,0\,0 \\ 0 & 0 & -CC_y & CB2_y + CC_{y2} & 0 & 0 & 0\,0\,0\,0\,0\,0 \\ 0 & 0 & 0 & 0 & CC_z & -CC_z & 0\,0\,0\,0\,0\,0 \\ 0 & 0 & 0 & 0 & -CC_z & CC_z & 0\,0\,0\,0\,0\,0 \\ 0 & 0 & 0 & 0 & 0 & 0 & 0\,0\,0\,0\,0\,0 \\ 0 & 0 & 0 & 0 & 0 & 0 & 0\,0\,0\,0\,0\,0 \\ 0 & 0 & 0 & 0 & 0 & 0 & 0\,0\,0\,0\,0\,0 \\ 0 & 0 & 0 & 0 & 0 & 0 & 0\,0\,0\,0\,0\,0 \\ 0 & 0 & 0 & 0 & 0 & 0 & 0\,0\,0\,0\,0\,0 \\ 0 & 0 & 0 & 0 & 0 & 0 & 0\,0\,0\,0\,0\,0 \end{bmatrix}. \tag{12}$$

It is quite common to describe the structural damping matrix $[C_s]$ of the system by a matrix that is proportional to the mass and the stiffness matrices, which can be expressed as

$$[C_s] = a[M] + b[K], \tag{13}$$

where a and b are the constants; according to [25], they have the following values: $a = 5$ and $b = 1.35 \times 10^{-5}$, respectively.

The following expression describes the total damping effect:

$$[C] = [C_{st}] + [C_v], \tag{14}$$

where $[C_{st}]$ is the structural damping matrix, $[C_v]$ is the viscous damping matrix, and $[C]$ is the total damping matrix

The model of the rotor-coupling-bearing system has several assumptions that apply throughout this paper:

(i) Both shafts were connected to the coupling by an interference fit to avoid introducing keys to the system

(ii) The bearings did not impose any longitudinal stiffness or damping

(iii) The discs of the system are responsible for unbalance (introduced into the system as eccentricity in the excitation force equation)

(iv) The coupling's stiffness is independent of the angle of rotation

(v) The stiffness and damping coefficients of the coupling are fully described in three directions (one axial direction and two radial directions)

(vi) Imbalance and misalignment are the only excitation forces in the system

(vii) The gyroscopic effect is neglected since the rotation speed is low (since less than 1000 rpm)

2.2. Modeling the Forces of Imbalance and Misalignment. The general arrangement of the coupled shafts with parallel and angular misalignments is shown in Figure 3.

The total misalignment ΔE is defined as the sum of the parallel misalignment Δy and the angular misalignment α, where O_1 and O_2 are the center of articulation for Subsystems 1 and 2, respectively:

$$\Delta E = \Delta y + \Delta L \tan(\alpha). \tag{15}$$

The excitation force that applies within the coupling is induced by two phenomena, which are the imbalance (denoted IB) and the misalignment (denoted MA). Therefore, the vector force has two components:

$$\{\mathbf{F}(\mathbf{t})\} = \{\mathbf{F_{IB}}(\mathbf{t})\} + \{\mathbf{F_{MA}}(\mathbf{t})\}. \tag{16}$$

2.2.1. Forces due to Imbalance. The imbalance force is related to the dynamic eccentricity of the system that appears in the two parts of the coupling. The radial imbalance force can be defined as follows:

$$F_{UB}(t) = \begin{bmatrix} F_{x1} = m_1 e_1 \omega^2 \sin(\omega t + \phi) \\ F_{x2} = m_2 e_2 \omega^2 \sin(\omega t + \phi) \\ F_{y1} = m_1 e_1 \omega^2 \cos(\omega t + \phi) \\ F_{y2} = m_2 e_2 \omega^2 \cos(\omega t + \phi) \\ F_{z1} = 0 \\ F_{z2} = 0 \\ F_{\theta 1} = \dfrac{I_{z1}}{r} e_1 \omega^2 \sin(\omega t + \phi) \\ F_{\theta 2} = \dfrac{I_{z2}}{r} e_2 \omega^2 \sin(\omega t + \phi) \\ F_{\beta 1} = 0 \\ F_{\beta 2} = 0 \\ F_{\gamma 1} = 0 \\ F_{\gamma 2} = 0 \end{bmatrix}, \tag{17}$$

where e_1 is the mass eccentricity of Subsystem 1, e_2 is the mass eccentricity of Subsystem 2, ω is the rotational speed of the shafts, t is the time, r is the radius of eccentricity in the coupling, and ϕ is the phase between the imbalance and the misalignment forces.

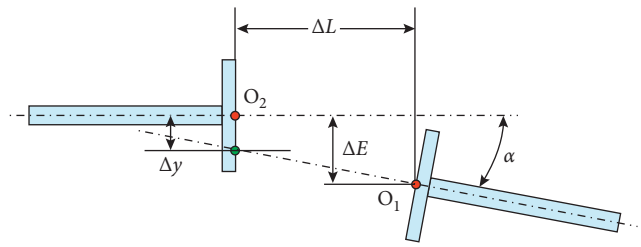

Figure 3: Model of misalignment modeling between Subsystems 1 and 2.

2.2.2. Forces due to Parallel Misalignment. Misalignment is not easy to detect on machinery that is running. The radial forces transmitted from one shaft to another, through a coupling, are typically combination of static (i.e., unidirectional) and dynamic forces that are difficult to measure externally. Unfortunately, outside evaluation of how much force is being applied to the couplings is practically unavailable.

In the literature, the attempts to theoretically describe and quantify the internal forces inside a coupling are relatively limited. Because of the difference in the internal geometry, a theoretical model developed for a particular type of coupling is generally not suitable for other types. Of particular interest is the theoretical model developed by Wang and Jiang [24], for a disc coupling, and refined by Wang and Gong [25].

As developed in [25], in the case of a parallel misalignment, the radial forces F_{x1} and F_{y1} on the right-hand side of the coupling are expressed as

$$\begin{aligned} F_{x1} &= F\sin(\omega t) = K_x \frac{\Delta E}{2}\cos(\omega t)\sin(\omega t) \\ &= K_x \frac{\Delta E}{4}\sin(2\omega t), \end{aligned} \tag{18}$$

$$\begin{aligned} F_{y1} &= F\cos(\omega t) = K_y \frac{\Delta E}{2}\cos(\omega t)\cos(\omega t) \\ &= K_y \frac{\Delta E}{4}(1 + \cos 2\omega t), \end{aligned} \tag{19}$$

where K_x and K_y are the coupling stiffness in the x and y directions, respectively, and ΔE is the total misalignment.

In the previous equations, one can see that for the developed expressions, as expected beforehand, the force in the x direction is harmonic. At the same time, the one in the y direction, because of the supporting condition in that direction, is a combination of static and harmonic components. Moreover, in both directions, the forces are pulsating with double the rotation frequency, i.e., the radial forces change two times their directions for one rotation cycle of the coupling.

The radial forces on the left-hand side of the coupling are simply the opposite of the opposite side:

$$F_{x2} = -F_{x1}, \tag{20}$$

$$F_{y2} = -F_{y1}. \tag{21}$$

2.2.3. Forces due to Angular Misalignment. The angular misalignment forces were derived by following the methodology of Xu and Marangoni [12] and Wang and Gong [25]. Figure 4 illustrates the torque decomposition of the coupling subsystems in which an angular misalignment fault is present.

The driving torque T, from the motor, splits into two components, T_Z and T_R, when it passes through the misaligned coupling, as shown below:

$$T_R = T\sin\alpha, \tag{22}$$

$$T_z = T\cos\alpha. \tag{23}$$

The torque component T_z is along the rotor axis, while the component T_R is perpendicular, causing lateral shaft bending deflection. The bending moment T_R can be decomposed into two components, in the x and y directions, which can be expressed as follows:

$$\begin{aligned} T_x &= T\sin\alpha\cos(\omega t), \\ T_y &= T\sin\alpha\sin(\omega t). \end{aligned} \tag{24}$$

As mentioned by Xu and Marangoni [12] and Wang and Gong [25], the ratio of the relative velocity between the misaligned shafts is calculated as

$$\frac{\omega_2}{\omega_1} = \frac{C_1}{1 + C_2\cos 2\omega t}, \tag{25}$$

where

$$\begin{aligned} C_1 &= \frac{4\cos\alpha}{3 + \cos 2\alpha}, \\ C_2 &= \frac{1 - \cos\alpha}{3 + \cos 2\alpha}. \end{aligned} \tag{26}$$

By differentiating equation (25) and making minor rearrangements, we can obtain an expression for the acceleration at Node 2 as follows:

$$\ddot{\theta} = \frac{2C_1C_2\,\omega^2\sin 2\omega t}{\left(1 + C_2\cos 2\omega t\right)^2}. \tag{27}$$

Next, the torque caused by angular misalignment is calculated via the following equation:

$$T_Z = I_Z\ddot{\theta} = I_Z\,\frac{2C_1C_2\,\omega^2\sin 2\omega t}{\left(1 + C_2\cos 2\omega t\right)^2}. \tag{28}$$

Consequently, the torques in the x and y directions are expressed as

$$\begin{aligned} T_x &= I_Z\tan\alpha\,\frac{2C_1C_2\,\omega^2\sin 2\omega t}{\left(1 + C_2\cos 2\omega t\right)^2}\cos\omega t, \\ T_y &= I_Z\tan\alpha\,\frac{2C_1C_2\,\omega^2\sin 2\omega t}{\left(1 + C_2\cos 2\omega t\right)^2}\sin\omega t. \end{aligned} \tag{29}$$

The misalignment force vector for parallel and angular misalignments is defined as follows:

$$F_{\mathrm{MA}}(t) = \begin{bmatrix} F_{x1} = +K_x\dfrac{\Delta E}{4}\sin(2\omega t) \\ F_{x2} = -K_x\dfrac{\Delta E}{4}\sin(2\omega t) \\ F_{y1} = +K_y\dfrac{\Delta E}{4}(1 + \cos 2\omega t) \\ F_{y2} = -K_y\dfrac{\Delta E}{4}(1 + \cos 2\omega t) \\ F_{y2} = -K_y\dfrac{\Delta E}{4}(1 + \cos 2\omega t) \\ F_{z1} = 0 \\ F_{z2} = 0 \\ F_{\theta1} = +I_{Z2}\dfrac{2C_1C_2\omega^2\sin 2\omega t}{\left(1 + C_2\cos 2\omega t\right)^2} \\ F_{\theta2} = -I_{Z2}\dfrac{2C_1C_2\omega^2\sin 2\omega t}{\left(1 + C_2\cos 2\omega t\right)^2} \\ F_{\beta1} = +F_{\theta1}\tan\alpha\cdot\cos\omega t \\ F_{\beta2} = -F_{\theta1}\tan\alpha\cdot\cos\omega t \\ F_{\gamma1} = +F_{\theta1}\tan\alpha\cdot\sin\omega t \\ F_{\gamma2} = -F_{\theta1}\tan\alpha\cdot\sin\omega t \end{bmatrix}, \tag{30}$$

2.3. Determination of Flexible Coupling Stiffness. The two couplings used in this study are aluminum spiral couplings (Figure 5), with an outer diameter of 24/16 inches (38.1 mm) and an inner diameter of 10/16 inches (15.875 mm). These are named the "*white*" and "*black*" couplings due to the color of their coatings. The two couplings are similar in all aspects apart from the length and degree of their spiral grooves. The white coupling has 380° grooves, while the black coupling has 525° grooves.

The coupling flexibility influences the dynamics of the rotatory system, especially under misalignment conditions. The ability of a flexible coupling to accommodate misalignment is a vital feature to reach desired performance in terms of vibrational behavior. Therefore, accurate estimation or measurement of the coupling stiffness is always a fundamental step in any theoretical or numerical investigation. The stiffness values of the actual couplings were estimated by FE simulations, as portrayed in Figure 6. The stiffness of the coupling in a specific direction is calculated by correlating

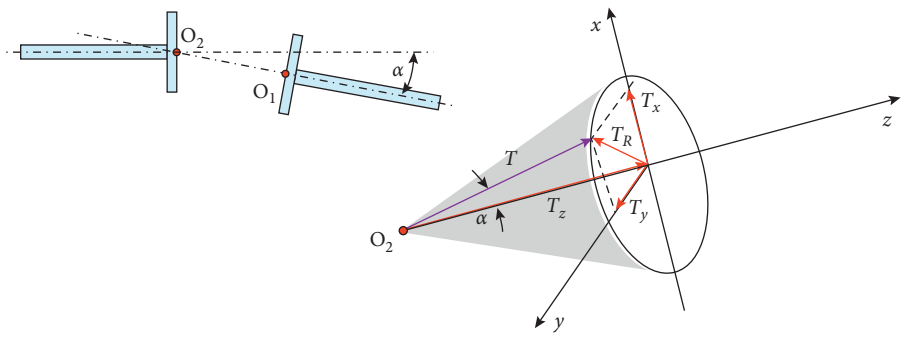

Figure 4: Torque decomposition of coupled shafts in which angular misalignment is present.

Figure 5: The flexible spiral couplings used in this investigation.

the load applied in that direction with the resulting deflection in the same direction. The torsional stiffness is obtained in a similar way, except for the load, which is replaced by a moment.

The reliability of any modeling process depends not only on the development of the model itself but also on the numerical values of its physical parameters. Therefore, it is necessary to obtain accurate and realistic values obtained via FE analysis. As a first check, some of the simulation results for the white coupling were compared with the available data provided by the manufacturer [29]. The comparison displayed in Table 1 shows a reasonable degree of matching between both sets of results.

The linear and torsional stiffness values of the white coupling resulting from the FE simulation are summarized in Table 2.

2.4. Determination of the Coupling's Damping Coefficients. The damping values of the coupling in three directions were obtained experimentally by conducting an impact test with a PCB PIZOTRONICS impact hammer (Model PCB-086, 0–500 lb, 10 mV/lb), an ICP accelerometer (Model No. 352C33, 100 mV/g), and a BETAVIB data acquisition unit, as displayed in Figure 7. The results are summarized in Table 3.

2.5. Stiffness and Damping of the Bearings and Shaft. The bearing's stiffness and damping values were estimated in accordance with the previous work of Badri [30]. The longitudinal, lateral, and torsional stiffness values of the shafts were obtained by applying the laws of solid mechanics.

2.6. Numerical Solution of the Equations of Motion for the Rotor-Coupling-Bearing System. To solve the equations of motion numerically, a Matlab code was created to compute the model's states by applying an explicit Runge–Kutta (4,5) formula for numerical integration. The parameters of the rotor-coupling-bearing system used in the numerical solution for the white coupling are listed in Tables 4–6. Table 4 presents the parameters of the rotor-bearing system; the specific parameters of the white and black couplings are shown in Tables 5 and 6, respectively.

3. Results and Discussion

This section presents the simulation results for the rotor-coupling-bearing system and discusses the findings. In the simulation that examined the model's response to imbalance and misalignment forces, the white coupling was used. The simulation results are presented and analyzed in the time and frequency domains. In the time domain, the results are given up to the limit of 0.5 seconds, which allows visualizing ten cycles of vibration. The results are displayed up to 100 Hz in the frequency domain, as this is the range that encloses 1X, 2X, 3X, and 4X.

3.1. Effect of Pure Imbalance on the Vibration Response. The effect of imbalanced forces on the vibration response of the rotor-coupling-bearing system was investigated in both the radial and angular directions.

3.1.1. Response to an Imbalance in the Radial Directions. The response of the system to an imbalance in the radial directions ($\mathbf{x}_1$, $\mathbf{x}_2$, $\mathbf{y}_1$, $\mathbf{y}_2$) was investigated at a rotation speed of 1200 rpm ($1\mathbf{X} = 20\,\mathbf{Hz}$). An eccentricity of 1 mm was introduced to the system in vertical and horizontal directions. Figure 8 shows the time- and frequency-domain responses in the x direction, and Figure 9 shows the responses in the y direction.

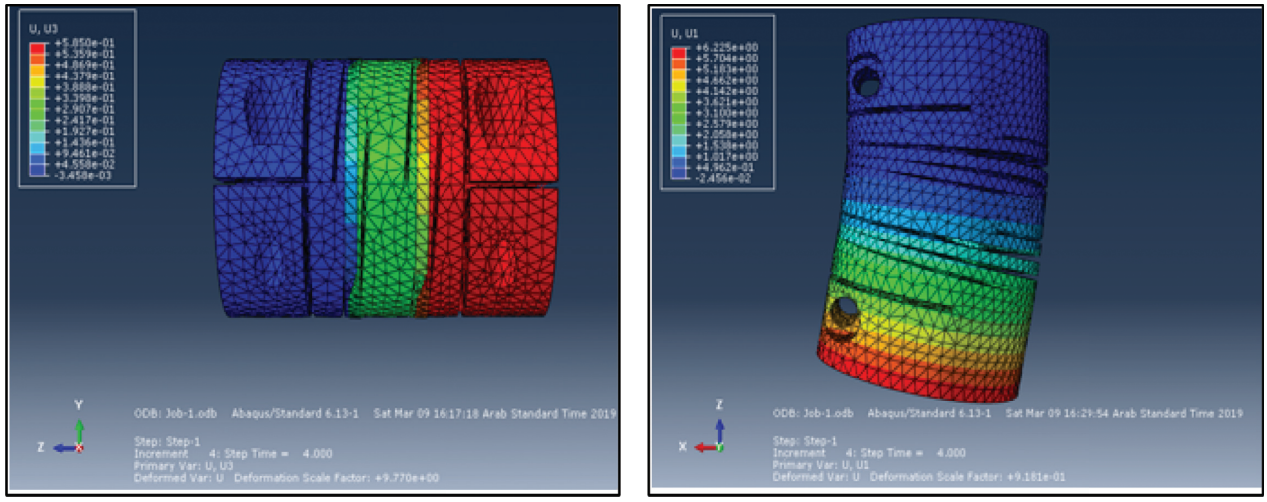

(a) (b)

Figure 6: Finite element analysis of the spiral coupling. (a) Tension and compression in the z direction. (b) Bending around the y direction.

Table 1: Physical parameters of the white coupling obtained by FE simulation versus the supplier's given data.

Physical parameters	Simulation result	Supplier data	Relative error (%)
Mass	134 g	130 g	3
Moment of inertia in the z direction	2.8185×10^{-5} kg/m^2	2.9937×10^{-5} kg/m^2	6

Table 2: Linear and torsional stiffness values of the coupling obtained by FE simulation.

Stiffness types	Stiffness values
Linear	k_x = 16.066 KN/m k_y = 16.122 KN/m k_z = 171.92 KN/m
Torsional	kT_x = 13.999 N.mm/rad kT_y = 13.928 N.mm/rad kT_z = 328.711 N.mm/rad

Figure 7: Experimental procedure used to find the coupling's damping values.

Table 3: Damping coefficients of the white coupling, as obtained experimentally.

Linear damping		
x direction	y direction	z direction
CC$_x$ = 3.42 Ns/m	CC$_y$ = 3.27 Ns/m	CC$_z$ = 5.65 Ns/m

As expected, the imbalanced excitation makes the system oscillate in a harmonic way that manifests itself as a pure sine wave in the time domain and a single peak in the frequency domain. The peak amplitudes of the displacement time responses appeared at 5.214×10^{-3} μm for the x_1 direction and 5.265×10^{-3} μm for the y_1 direction. The peak amplitude of the displacement time responses were 3.597×10^{-3} μm for the x_2 direction and 3.633×10^{-3} μm for the y_2 direction. Moreover, the vibrations at Node 1 are higher than those at Node 2 as expected because Subsystem 1 had a greater mass than Subsystem 2 (equations (17)–(23)). A slight change appeared between the amplitudes in the time and frequency domains, mainly caused by an error in the calculation of the fast Fourier transform (FFT) function in Matlab. Furthermore, the response of the time and frequency domains to displacement in the radial direction at Node 1 was almost constant, suggesting that the displacement responses of x_1 and y_1 directions are similar. The same was true for the displacement response at Node 2. This was expected because the stiffness and damping of the coupling, bearings, and shafts in the model were independent of both the vertical and horizontal directions.

3.1.2. The Unbalanced Response of the System in the Angular Direction. For the same conditions of speed (1200 rpm) and eccentricity (1 mm), the response of the system to an imbalance in the two angular directions (θ_1, θ_2) is displayed in Figure 10.

Table 4: Physical parameters of the rotor-bearing system.

Parameter	Value	Unit
$KB1_x$	6.56×10^8	N/m
$KB1_y$	6.56×10^8	N/m
$KB2_x$	6.56×10^8	N/m
$KB2_y$	6.56×10^8	N/m
$KS1_x$	1.28×10^6	N/m
$KS1_y$	1.28×10^6	N/m
$KS1_z$	3.43×10^8	N/m
$KS2_x$	7.27×10^6	N/m
$KS2_y$	7.27×10^6	N/m
$KS2_z$	6.12×10^8	N/m
$KS1T_z$	3790.15	N.m/rad
$KS2T_z$	6759.10	N.m/rad
$CB1_x$	1.8×10^3	N.s/m
$CB1_y$	1.8×10^3	N.s/m
$CB2_x$	1.8×10^3	N.s/m
$CB2_y$	1.8×10^3	N.s/m

Table 5: Physical parameters of the white flexible coupling.

Parameter	Value	Unit
m_1	0.21745	kg
m_2	0.15138	kg
I_{x1}	2.33×10^{-4}	kg.m^2
I_{x2}	4.90×10^{-5}	kg.m^2
I_{y1}	2.33×10^{-4}	kg.m^2
I_{y2}	4.88×10^{-5}	kg.m^2
I_{z1}	1.84×10^{-5}	kg.m^2
I_{z2}	1.66×10^{-5}	kg.m^2
KC_x	16066	N/m
KC_y	16122	N/m
KC_z	171920	N/m
KCT_x	13.999	N.m/rad
KCT_y	13.928	N.m/rad
KCT_z	328.711	N.m/rad
CC_x	3.42	N.s/m
CC_y	3.27	N.s/m
CC_z	5.65	N.s/m

Table 6: Physical parameters of the black flexible coupling.

Parameter	Value	Unit
m_1	0.21747	kg
m_2	0.14640	kg
I_{x1}	2.24×10^{-4}	kg.m^2
I_{x2}	4.68×10^{-5}	kg.m^2
I_{y1}	2.24×10^{-4}	kg.m^2
I_{y2}	4.66×10^{-5}	kg.m^2
I_{z1}	1.74×10^{-5}	kg.m^2
I_{z2}	1.55×10^{-5}	kg.m^2
KC_x	6422.6	N/m
KC_y	6472.4	N/m
KC_z	52315	N/m
KCT_x	6.577	N.m/rad
KCT_y	6.506	N.m/rad
KCT_z	125.923	N.m/rad
CC_x	1.62024	N.s/m
CC_y	1.59528	N.s/m
CC_z	1.39776	N.s/m

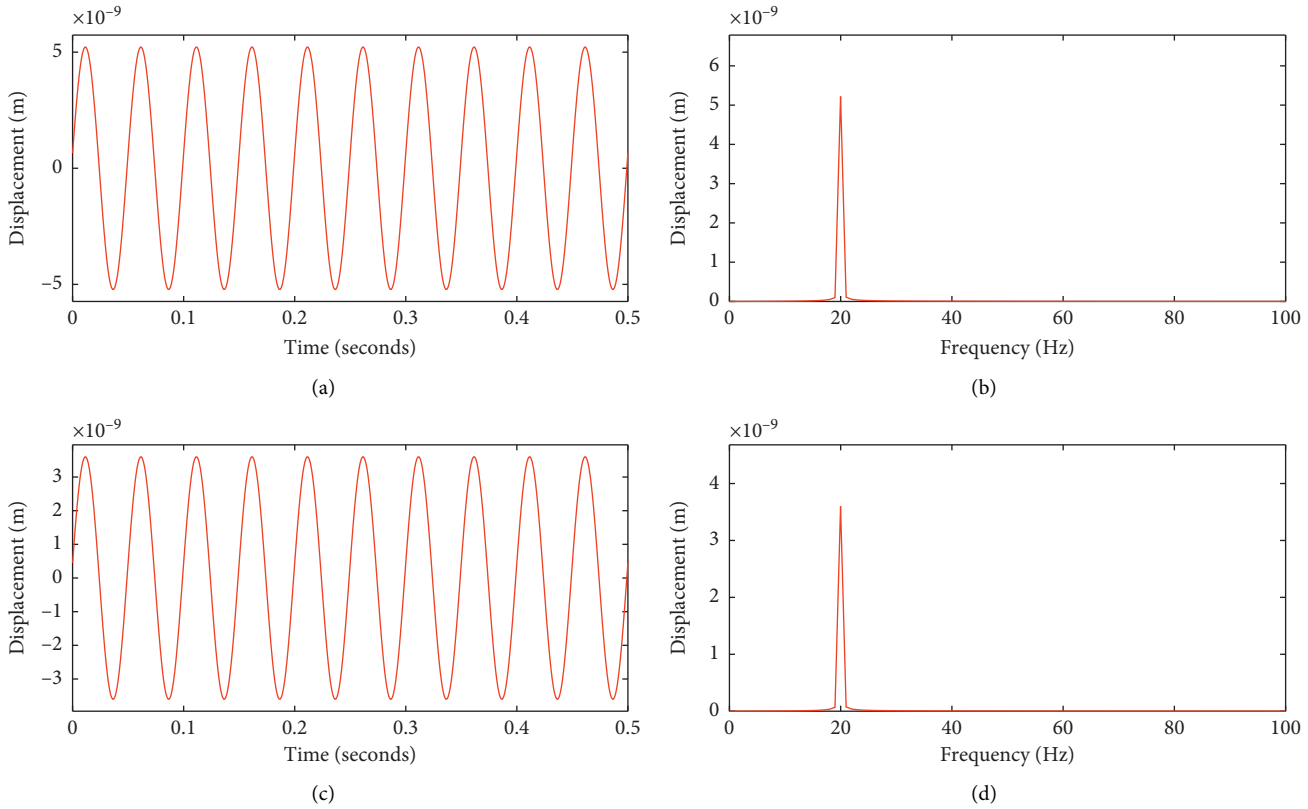

Figure 8: Response of the time and frequency domains to an imbalance in the x direction. (a) Time response of x1. (b) Frequency response of x1. (c) Time response of x2. (d) Frequency response of x2.

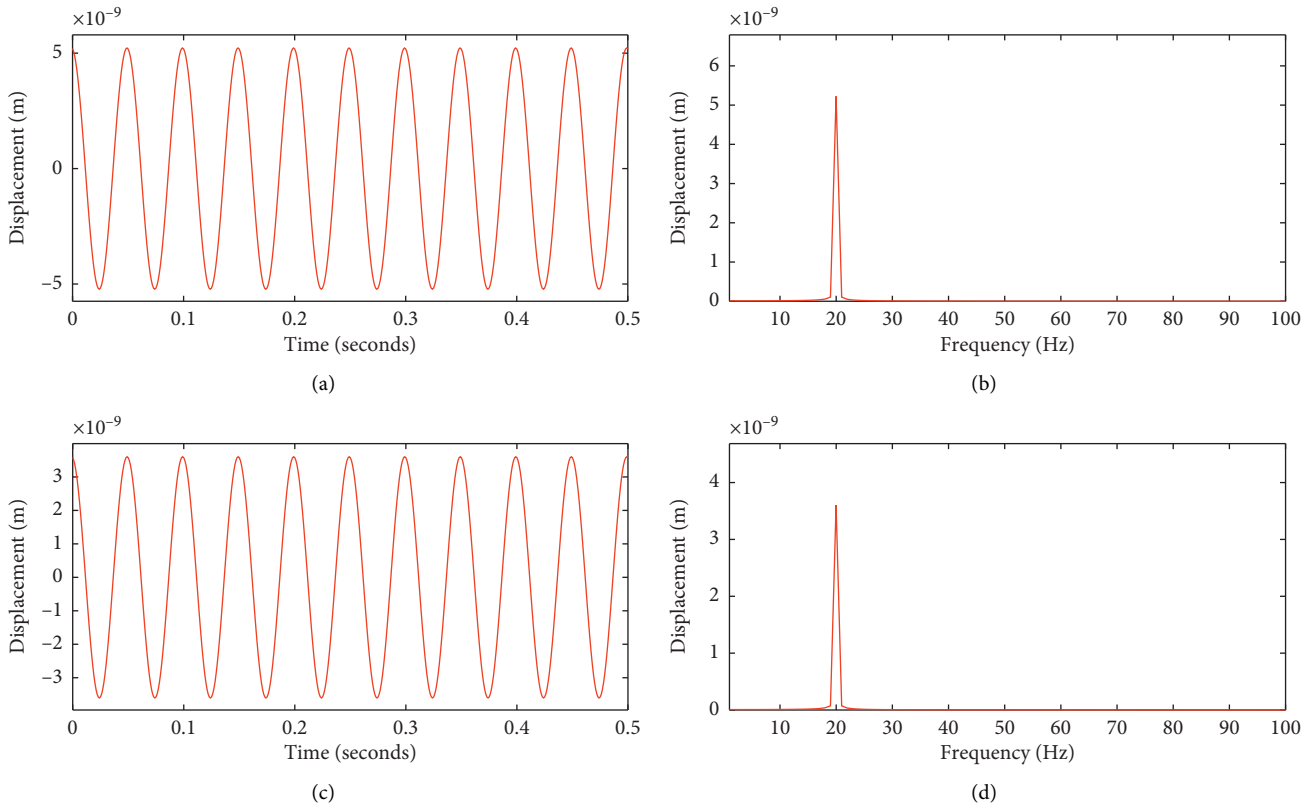

Figure 9: Response of the time and frequency domains to an imbalance in the *y* direction. (a) Time response of y1. (b) Frequency response of y1. (c) Time response of y2. (d) Frequency response of y2.

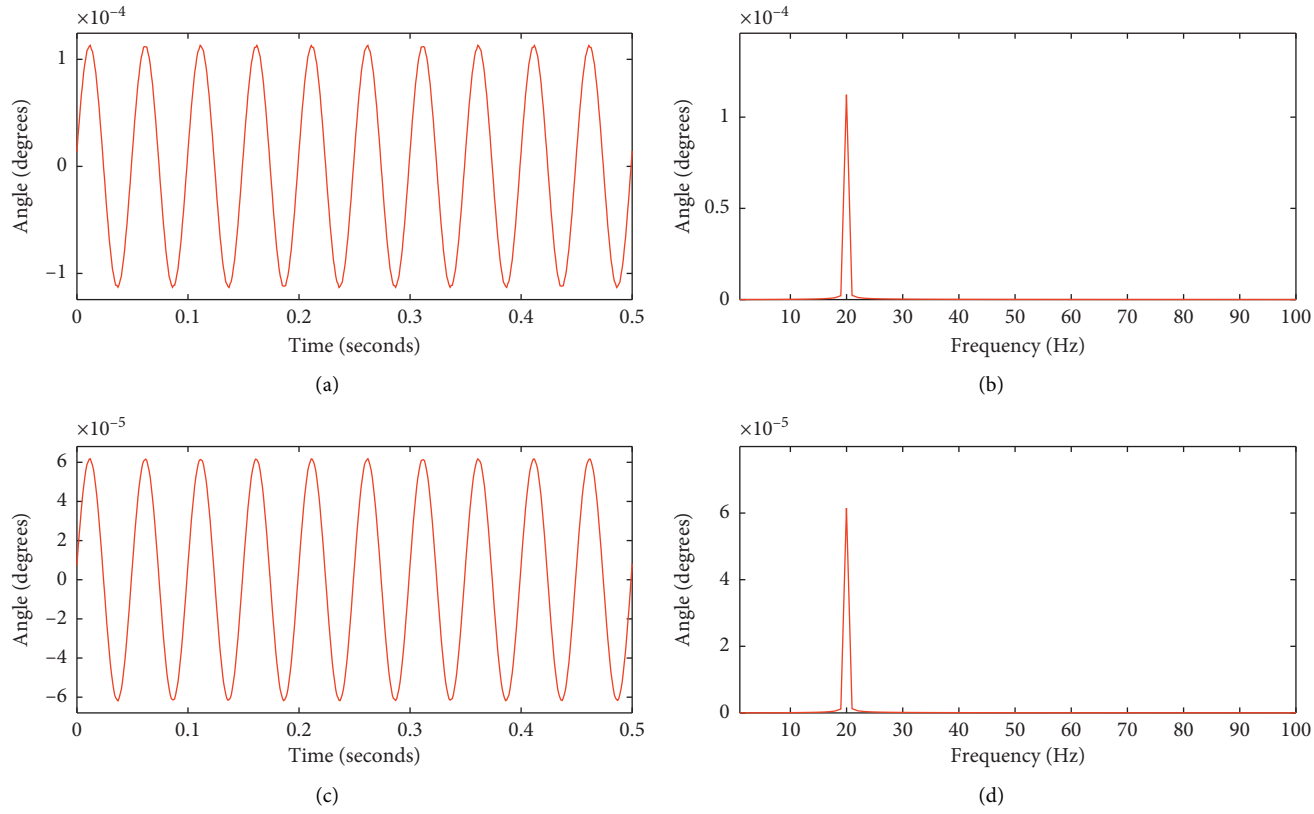

Figure 10: Time- and frequency-domain response of the unbalanced system in angular directions θ_1 and θ_2. (a) Time response of θ_1. (b) Frequency response of θ_1. (c) Time response of θ_2. (d) Frequency response of θ_2.

Once more, the response is harmonic. It manifests as a sinusoidal curve in the time domain and a single peak centered at 1X in the frequency domain.

3.2. Vibration Response to the Combined Effects of Imbalance and Parallel Misalignment. Parallel misalignment has a strong influence on the vibration response of all rotating assembly systems. In this section, a particular case of a 1 mm imbalance, combined to the simultaneous effect of a 1 mm gap of parallel misalignment, was simulated and analyzed. The system was supposed to rotate at the same speed (1200 rpm). Figures 11 and 12 present the responses in the time and frequency domains to faults in the radial directions x and y.

In Figures 11 and 12 , the time-domain plots are no longer harmonic, but rather periodic. In the frequency domain, instead of a single peak, two peaks are now dominating the spectrum. The first one is the fundamental frequency of the rotating assembly (1X), and the second one is its second harmonic (2X).

Although the time domain's waveform changed considerably in both radial directions (x and y), one can see that the amplitudes of $\mathbf{x}_1$ and $\mathbf{y}_1$ at Node 1 and $\mathbf{x}_2$ and $\mathbf{y}_2$ at Node 2 are comparable. This can be explained by the same arguments as for pure imbalance, previously described in Section 3.1.1. Table 7 shows the peak amplitudes in the radial direction obtained from the spectrum.

If we admit that the first peak (1X) is related to imbalance and the second peak (2X) is related to misalignment, the results reported in Table 7 clearly show that the amplitude of 2X is much more sensitive to parallel misalignment. This finding confirms the results already known to and widely accepted by many practitioners and researchers (Section 1.3).

Moreover, the amplitude of 2X is almost constant in all directions. This is probably a result of the model properties being similar in those directions.

3.2.1. Effect of Varying the Amount of Parallel Misalignment. The next step in our investigation of misalignment was to alter the degree of parallel misalignment and analyze the effects on the dynamic behavior of the rotor-coupling-bearing system. To pursue this inquiry, a set of parallel misalignment values, ranging from 0.2 mm to 1.2 mm with a step of 0.2 mm, were included in the simulation model. During these simulations, the rotational speed was maintained at 1200 rpm. The results of this investigation are presented in Figure 13.

The results displayed in Figure 14(a) show that the amplitudes at Node 1 (for the right-hand side of the coupling) are higher than those at Node 2 (the left-hand side). Moreover, one can easily see that varying the parallel misalignment has practically no influence on the amplitude of the 1X peaks in all radial directions.

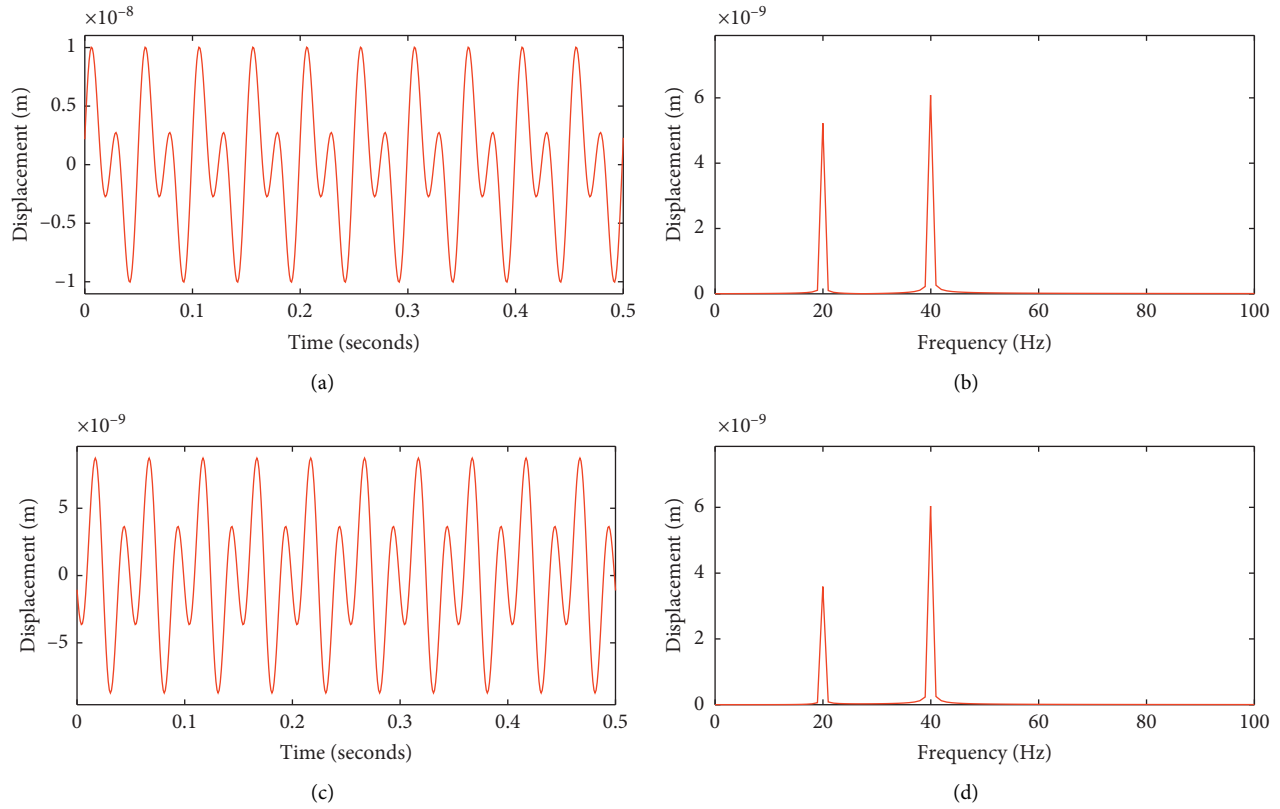

FIGURE 11: Time- and frequency-domain response of unbalance and parallel misalignment fault in the x directions (x_1 and x_2). (a) Time response of x1. (b) Frequency response of x1. (c) Time response of x2. (d) Frequency response of x2.

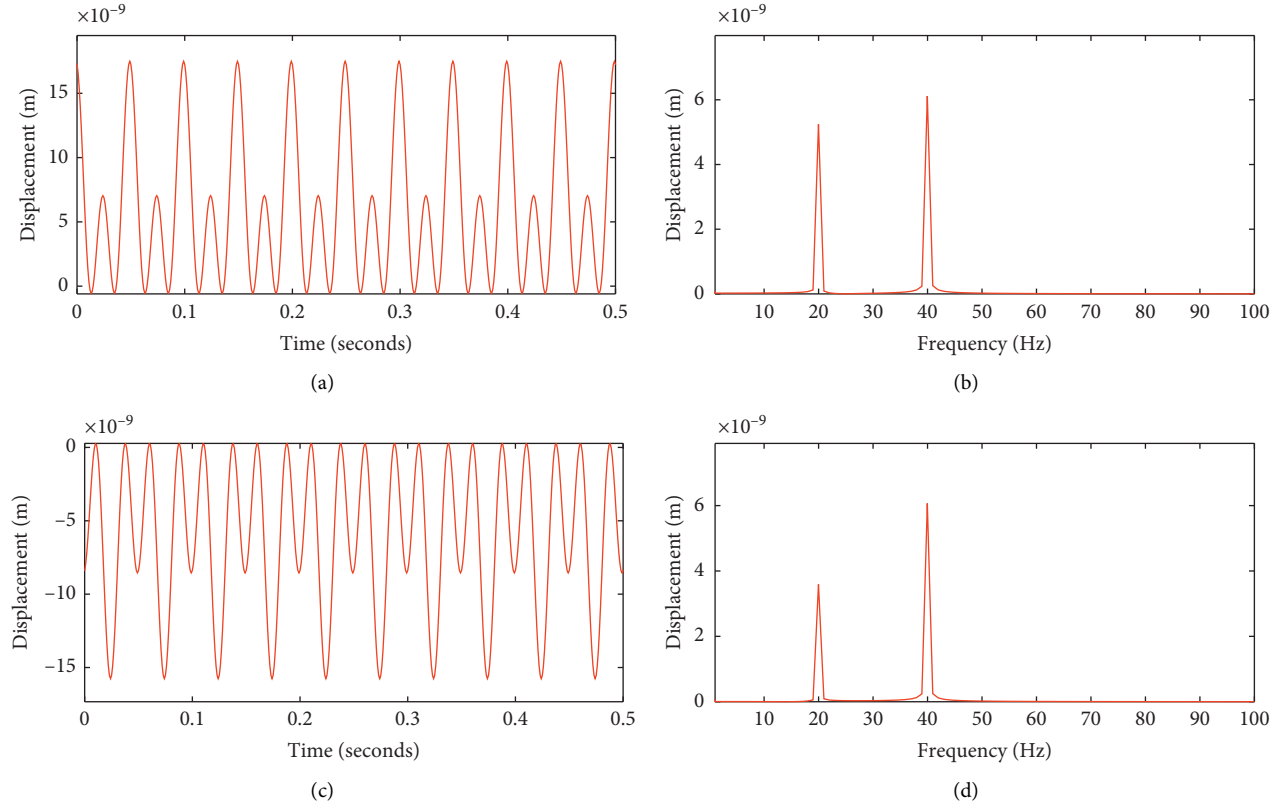

FIGURE 12: Time- and frequency-domain response in the x directions ($\mathbf{x}_1$ and $\mathbf{x}_2$), resulting from imbalance and parallel misalignment. (a) Time response of y1. (b) Frequency response of y1. (c) Time response of y2. (d) Frequency response of y2.

Table 7: Peak amplitudes of the fundamental and second harmonics in the radial direction.

Amplitude (μm)		$\mathbf{x}_1$	$\mathbf{x}_2$	$\mathbf{y}_1$	$\mathbf{y}_2$
Imbalance and parallel misalignment	$1\times$ rpm	5.226×10^{-3}	3.592×10^{-3}	5.240×10^{-3}	3.587×10^{-3}
	$2\times$ rpm	6.084×10^{-3}	6.041×10^{-3}	6.115×10^{-3}	6.066×10^{-3}
Pure imbalance	$1\times$ rpm	5.214×10^{-3}	3.597×10^{-3}	5.265×10^{-3}	3.633×10^{-3}
	$2\times$ rpm	0	0	0	0
% increase of $2\times$ rpm with respect to $1\times$ rpm		+16.4%	+68.2%	+16.7%	+69.1%

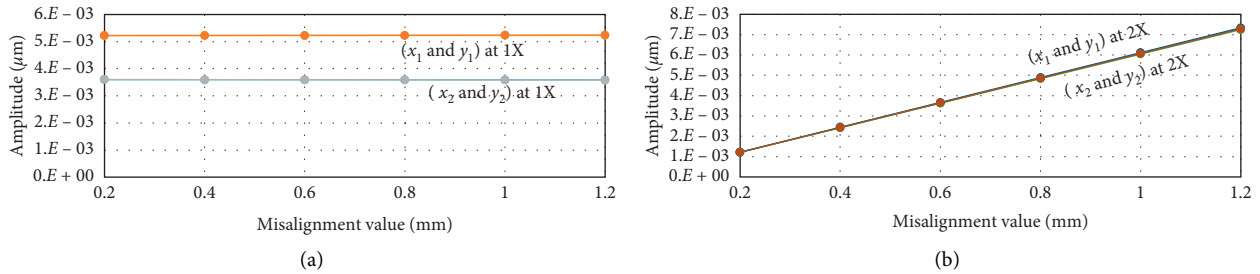

Figure 13: Effect of changing the extent of parallel misalignment on the vibration responses in the radial directions. (a) 1X; (b) 2X.

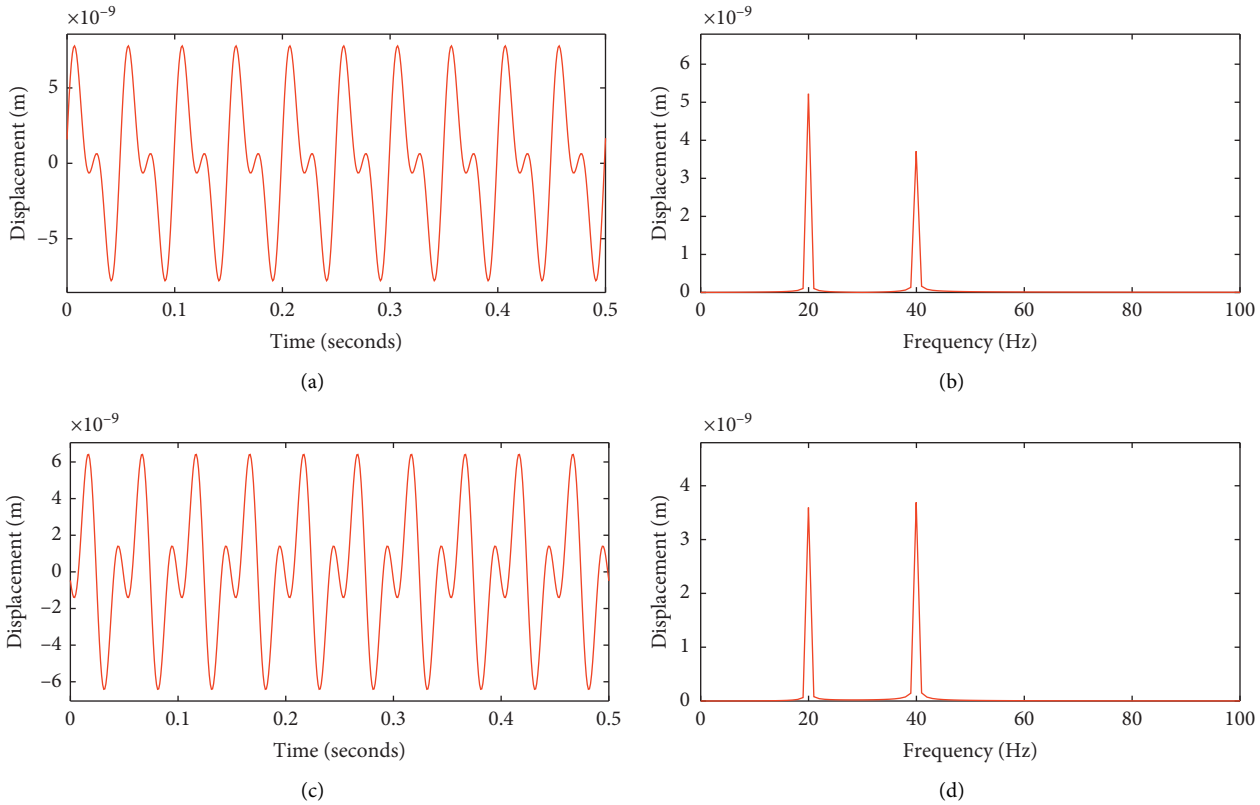

Figure 14: Time- and frequency-domain responses in the radial directions x_1 and x_2, under the combined effects of imbalance and angular misalignment. (a) Time response of x1. (b) Frequency response of x1. (c) Time response of x2. (d) Frequency response of x2.

However, the amplitude of the 2X peaks was found to increase linearly as the degree of parallel misalignment increased.

3.3. Vibration Response to the Combined Effect of Imbalance and Angular Misalignment. The goal of this section is to investigate the vibrations patterns emerging from a faulty

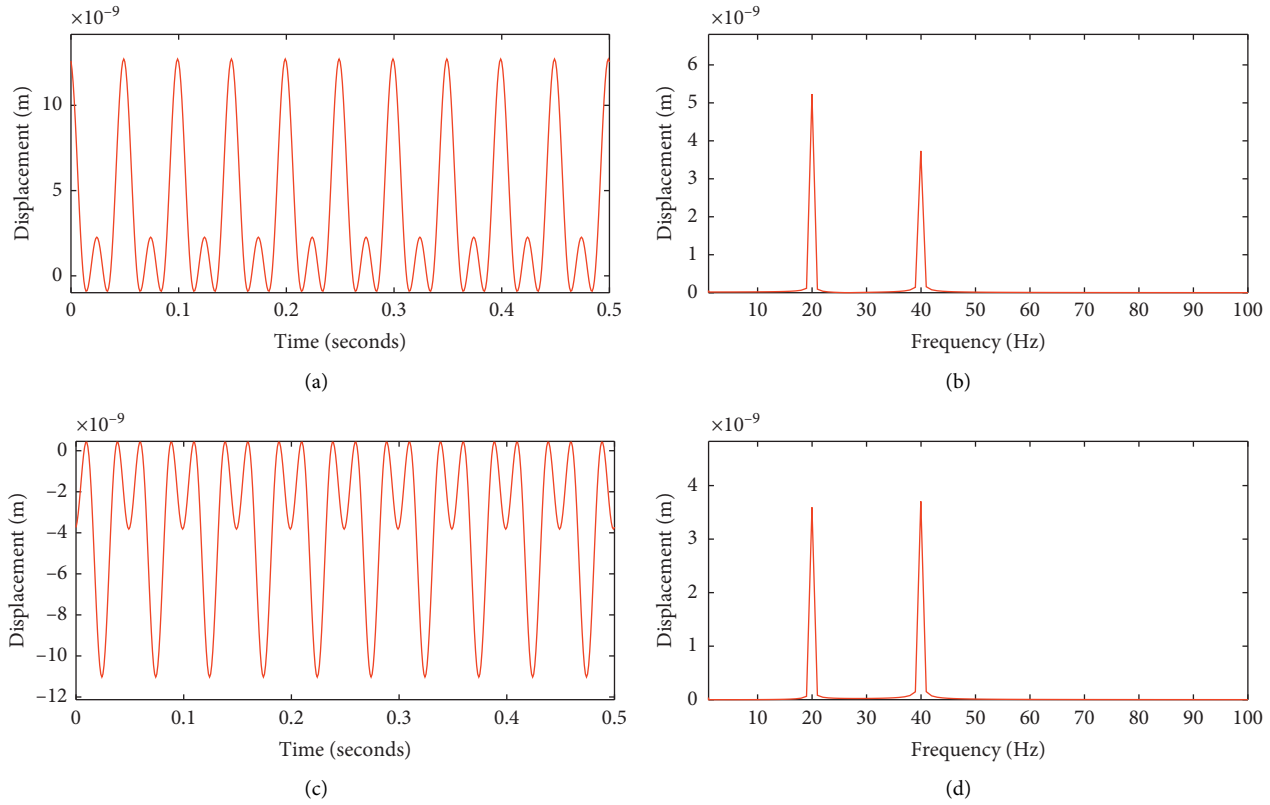

FIGURE 15: Time- and frequency-domain responses in the radial directions y_1 and y_2, under the combined effects of imbalance and angular misalignment. (a) Time response of y1. (b) Frequency response of y1. (c) Time response of y2. (d) Frequency response of y2.

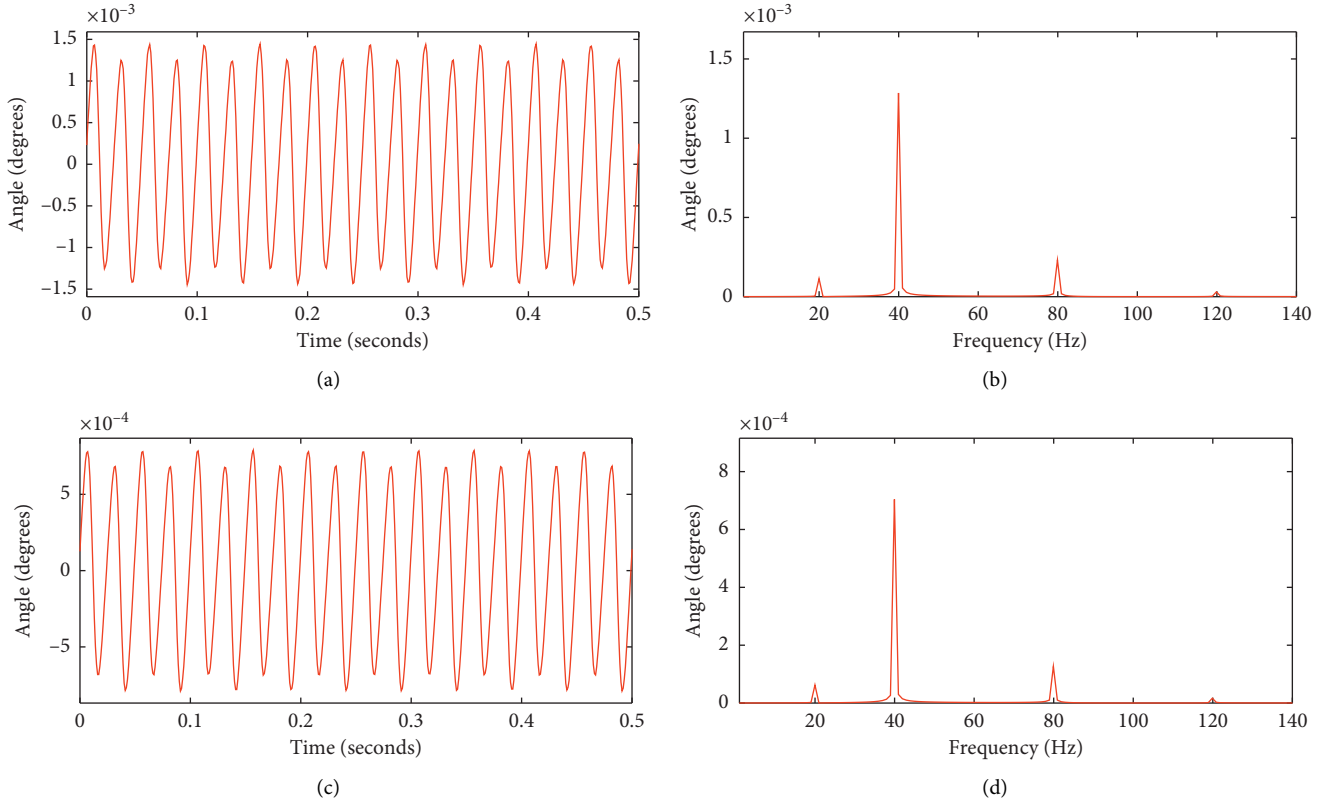

FIGURE 16: Time- and frequency-domain responses to the combined effects of imbalance and angular misalignment in the angular directions θ_1 and θ_2. (a) Time response of θ_1. (b) Frequency response of θ_1. (c) Time response of θ_2. (d) Frequency response of θ_2.

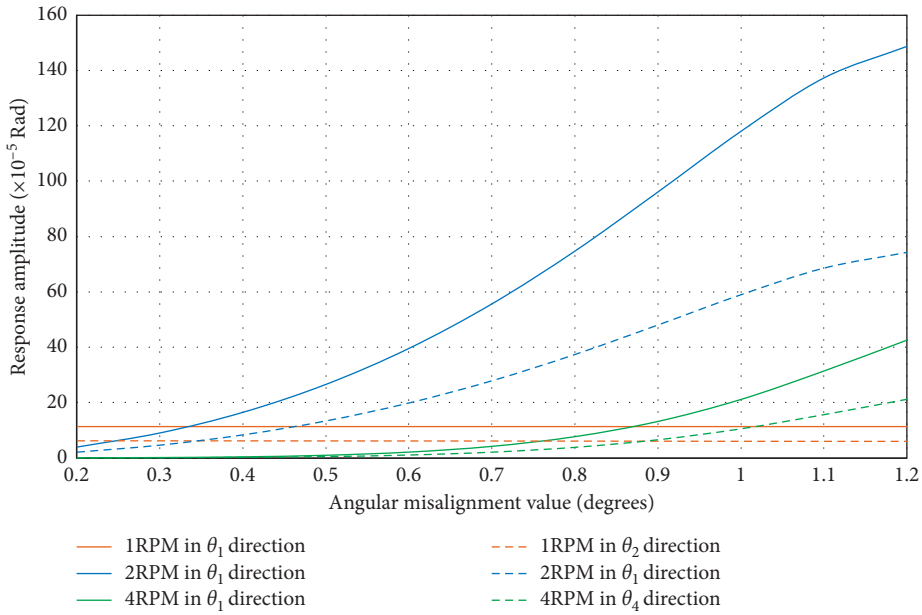

Figure 17: Effects of different degrees of angular misalignment on the vibration response.

Table 8: Peak amplitudes of the fundamental and second harmonics in the radial direction under the combined action of imbalance and angular misalignment.

Amplitude (μm)		$\mathbf{x}_1$	$\mathbf{x}_2$	$\mathbf{y}_1$	$\mathbf{y}_2$
Imbalance and angular misalignment	$1\times$ rpm	5.223×10^{-3}	3.595×10^{-3}	5.234×10^{-3}	3.593×10^{-3}
	$2\times$ rpm	3.714×10^{-3}	3.692×10^{-3}	3.735×10^{-3}	3.707×10^{-3}
Pure imbalance	$1\times$ rpm	5.214×10^{-3}	3.597×10^{-3}	5.265×10^{-3}	3.633×10^{-3}
	$2\times$ rpm	0	0	0	0
% increase of $2\times$ rpm with respect to $1\times$ rpm		−40.6%	+2.7%	−40.1%	+3.2%

Table 9: Angular spectrum of the system including imbalance and misalignment.

Amplitudes (in degrees)	θ_1	θ_2
$1\times$ rpm	0.1×10^{-3}	0.0595×10^{-3}
$2\times$ rpm	1.2×10^{-3}	0.5847×10^{-3}
$4\times$ rpm	0.2×10^{-3}	0.1051×10^{-3}

system when angular misalignment is present alongside imbalance. Once again, the rotational speed and the eccentricity value were kept identical to the previous cases (1200 rpm and 1 mm of eccentricity). However, in this case, an angular misalignment of 1° was introduced. Figures 15–17 display the new simulation results.

In conclusion, an angular misalignment of 1° was found to generate two comparable peaks at 20 Hz (1X) and 40 Hz (2X). The peak amplitudes in the radial direction obtained from the spectra are shown in Table 8.

Once again, the combined effect of imbalance and angular misalignment had the same effect on the amplitude of the fundamental peak (1X) as it did when the imbalance was acting alone. However, when a small angle of 1° was added to the mechanical system, this had a significant effect on the amplitude of the second harmonic of speed 2X.

The response in the angular directions θ_1 and θ_2, under the combined effects of imbalance and angular misalignment, is displayed in Figure 16.

At first glance, several comments could be made about the results. First, the noticeable difference in the time waveform shapes between radial and angular directions. Second, compared with the case of pure imbalance, one can see that the response of the time domain in the angular direction increased considerably because of one-degree angular misalignment. Remarkable 1X, 2X, and 4X frequency components can be observed in the amplitudes of the spectrum, with the 2X component being the strongest. Table 9 summarizes the peak amplitudes in this scenario.

In conclusion, a comparison between the case of a single defect (pure imbalance) and the case of combined defects (imbalance and angular misalignment) shows that the angular misalignment did not have a noticeable

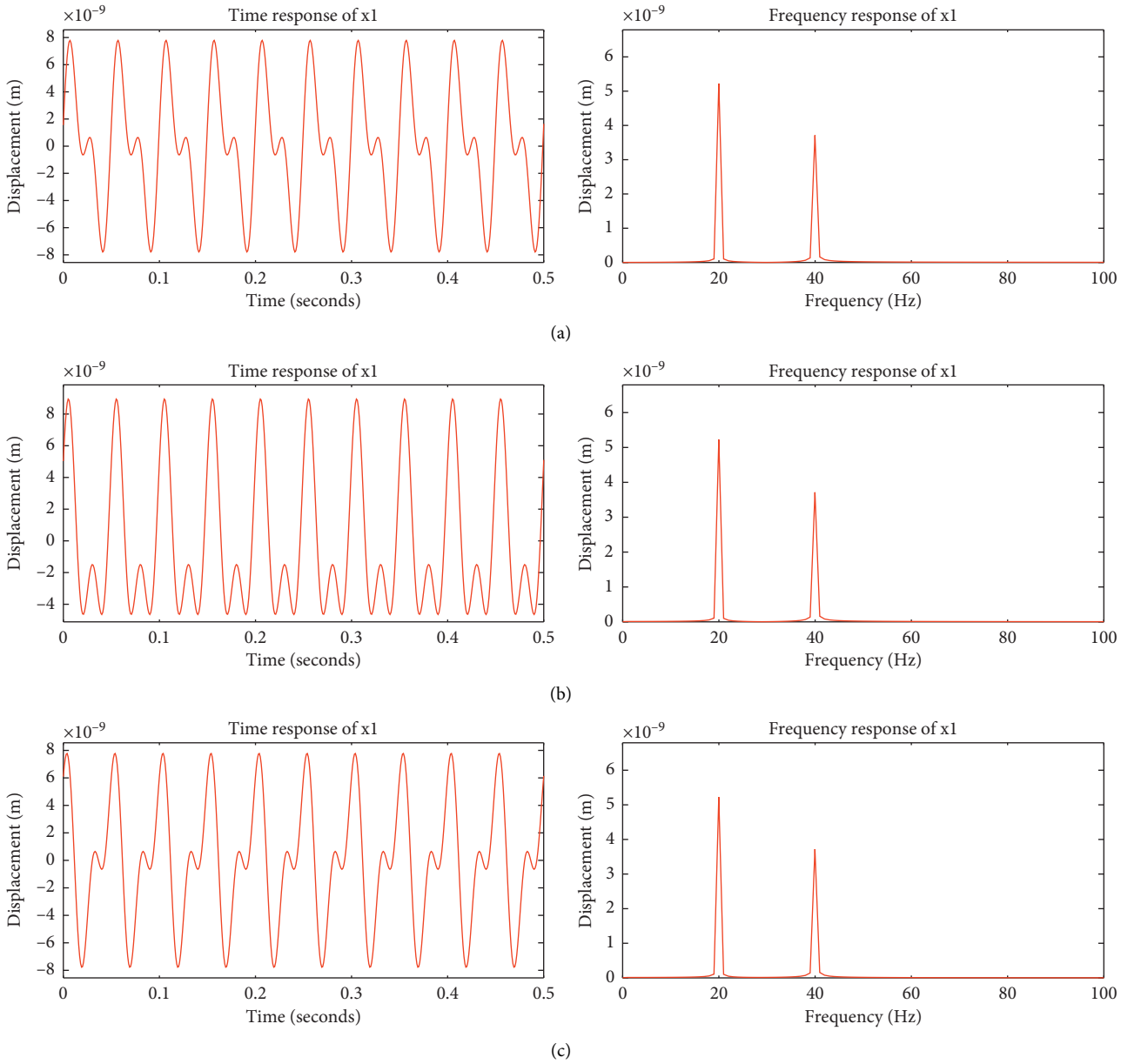

FIGURE 18: Effects of phase shift on the vibration response (time and frequency domains) in the radial direction x_1. (a) Phase = 0°. (b) Phase = 45°. (c) Phase = 90°.

effect on the amplitude of 1X. In contrast, the increase in the amplitude of 2X and 4X, noted in many previous studies (Section 1), was clearly visible. Unlike the case of parallel misalignment, the amplitudes of 2X and 4X were higher at Node 1 because of a more significant moment of inertia.

3.4. Effect of Varying the Angular Misalignment. Our next step in investigating misalignment was to change the degree of angular misalignment and examine its effects on the dynamic behavior of the rotor-coupling-bearing system.

A range of angular misalignment values was considered, from 0.2 to 1.2 degrees in steps of 0.2 degrees. For all simulations, the rotational speed remained at 1200 rpm. The simulation results are displayed in Figure 17.

Varying the angular misalignment had almost no effect on the amplitude of 1X. This peak is clearly related to imbalance. However, the angular misalignment could be recognized by the harmonics of the fundamental frequency (1X). The amplitudes of 2X and 4X increased as the degree of angular misalignment increased. In particular, the 2X component was the most sensitive, which confirms the findings of previous researches. Moreover, the amplitudes of 2X and 4X under angular misalignment were higher at Node 1 than at Node 2 because of the more significant moment of inertia in Subsystem 1 (equation (28)).

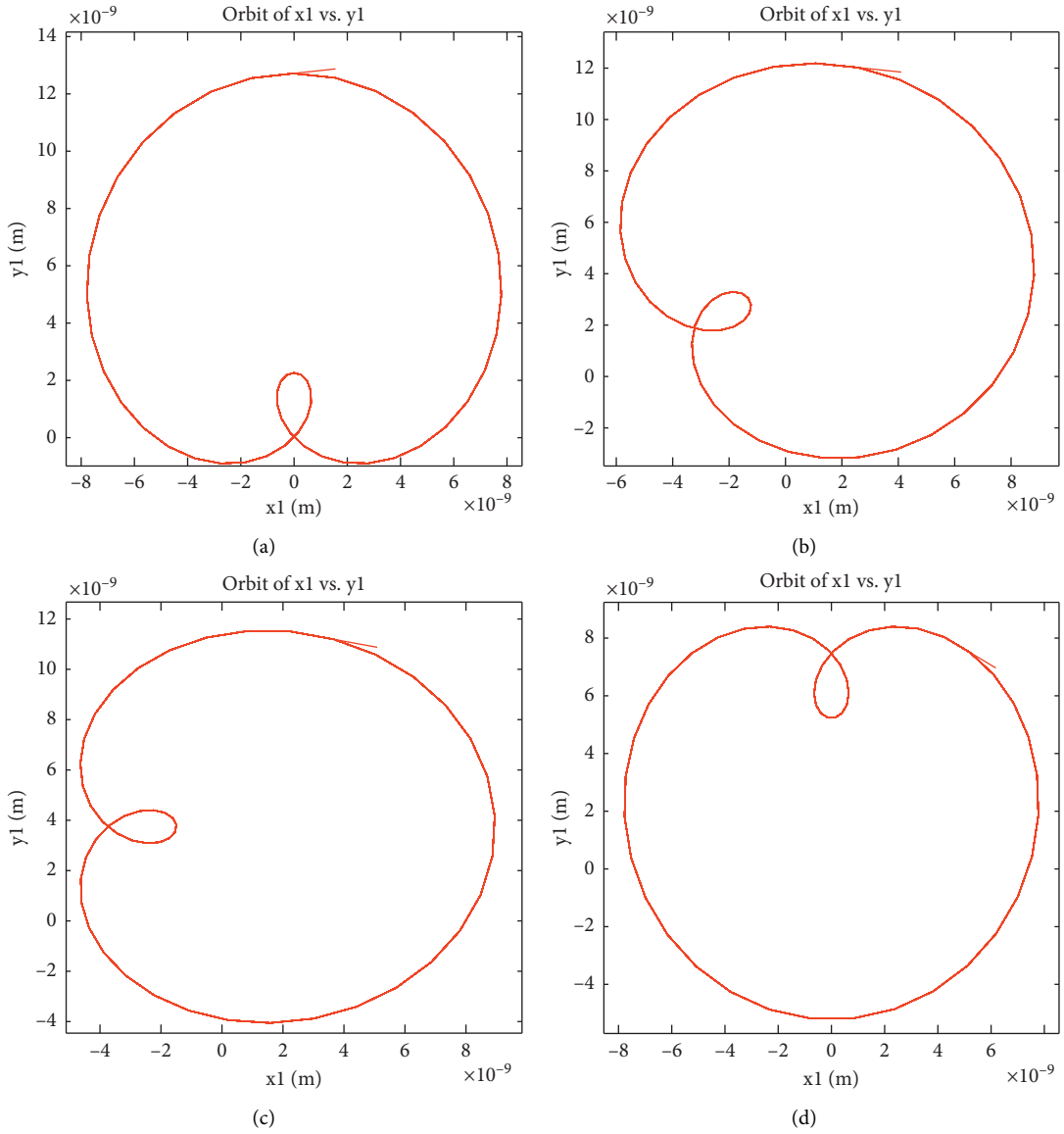

Figure 19: Effects of phase shift on the phase diagram between x_1 and x_2. (a) Phase = 0°. (b) Phase = 15°. (c) Phase = 45°. (d) Phase = 90°.

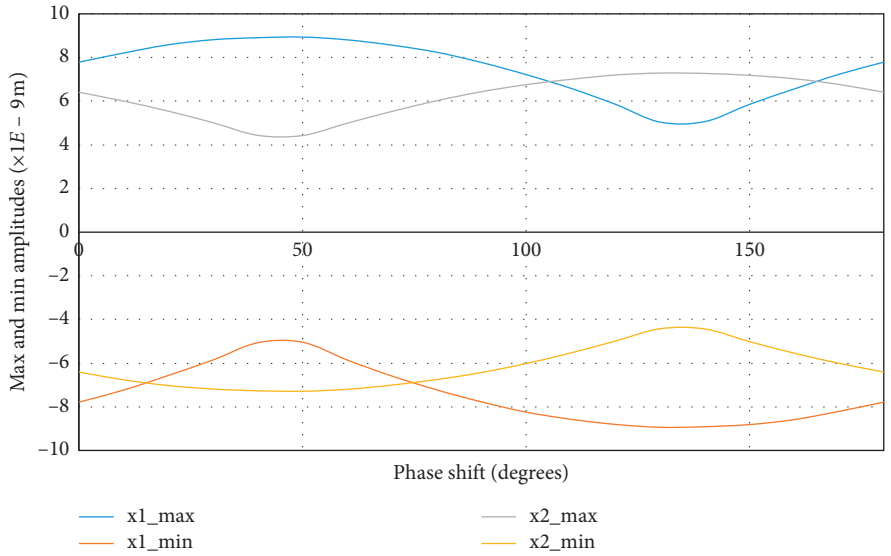

Figure 20: Effects of phase shift on the maximum and minimum amplitude values of x_1 and x_2.

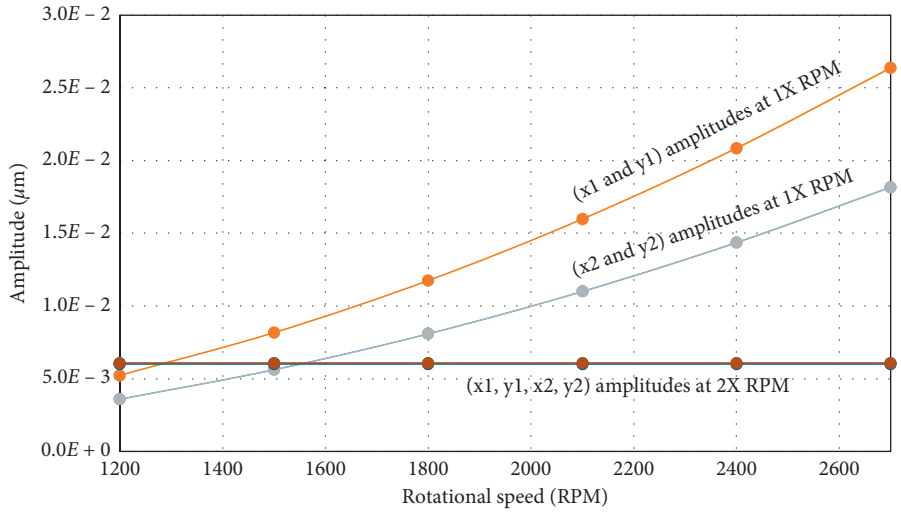

Figure 21: Effects of different rotational speeds on the vibration response of the system with imbalance and parallel misalignment.

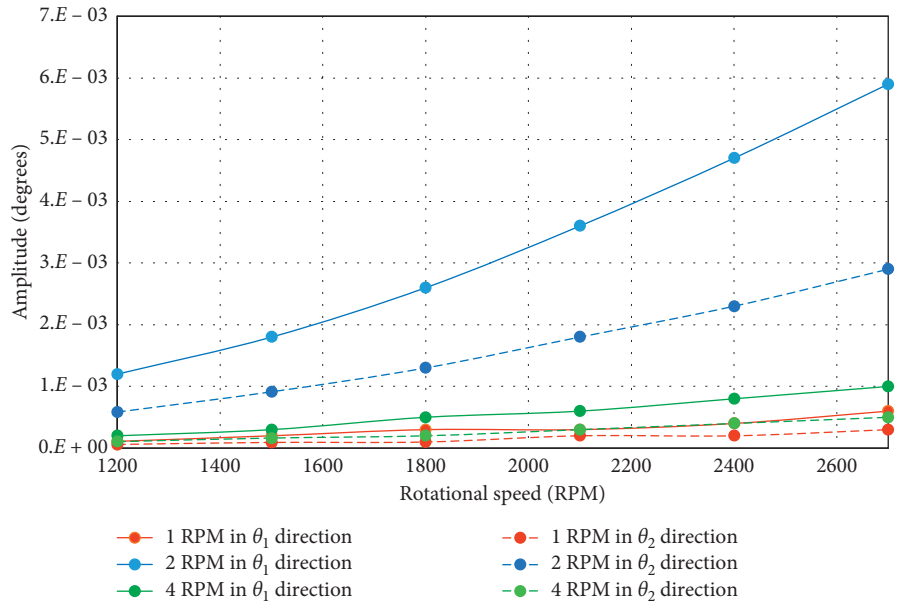

Figure 22: Effects of different rotational speeds on the vibration response of a system with imbalance and angular misalignment.

3.5. Effects of Changing the Shift of Phase between Imbalance and Misalignment. The phase relationship between the imbalance and the misalignment forces is investigated in this section. To pursue this inquiry, a set of phase values, ranging from 0 to 180°, were included in the simulation model. During these simulations, all other running conditions were maintained constant (the speed at 1200 rpm, imbalance eccentricity at 1 mm, angular misalignment at 1°, and no parallel misalignment). The results of this investigation are displayed in Figures 18–20.

Figure 18 displays the simulation response in the radial direction x_1, computed both in the time and the frequency domains. A stepped variation of the phase shift, introduced between the imbalance and the misalignment forces, is found to alter the shape of the time waveform significantly. Such an effect is not inflected to one particular direction, but rather to all of them. The phase diagram between x_1 and x_2 is a typical example of such effect. The orientation of the loop, displayed in Figure 19, is directly related to the amount of phase shift between the imbalance and misalignment. Moreover, a close look to x_1 and x_2 graphs reveals an obvious variation of their amplitudes. The simulation displayed in Figure 20 shows that, on a cycle of 180° variation of the phase shift, there is around 15% variation on x_1 and x_2 amplitudes.

3.6. Effects of Changing the Rotational Speed. To make our investigations into misalignment more thorough, we changed the rotational speed and examined the effects on the

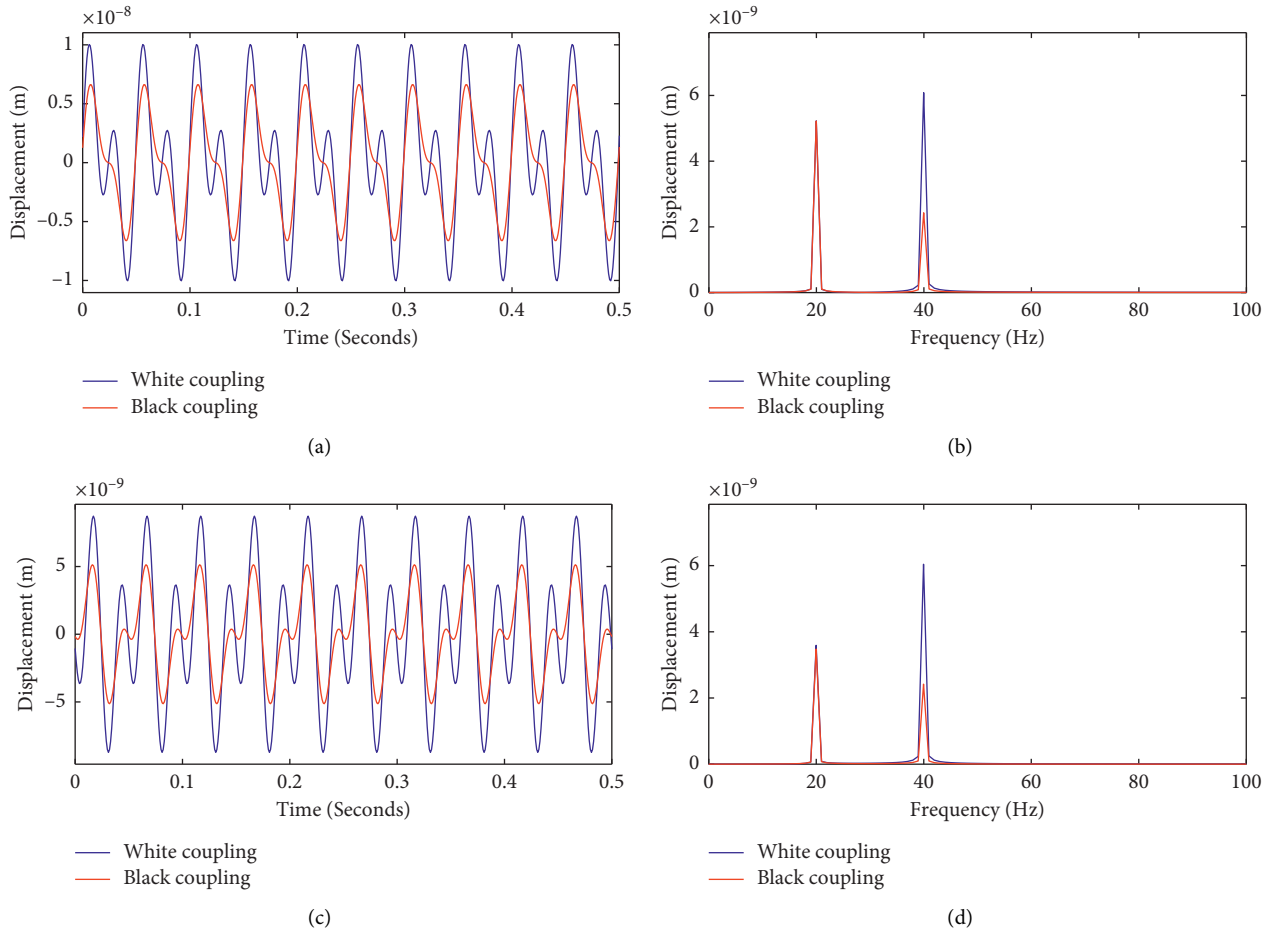

Figure 23: Effects of changing the coupling type in the x direction for a system with imbalance and parallel misalignment. (a) Time response of x1. (b) Frequency response of x1. (c) Time response of x2. (d) Frequency response of x2.

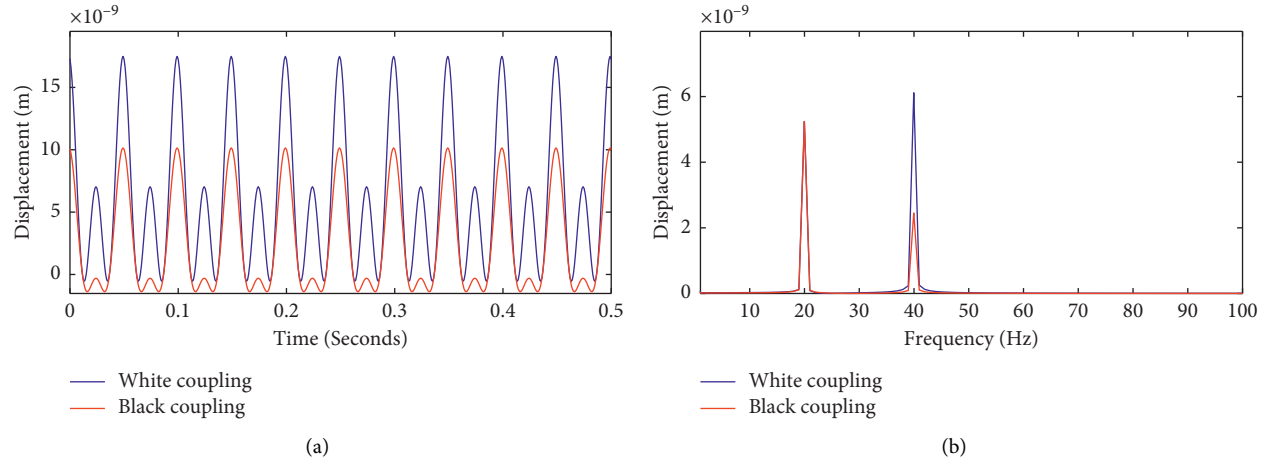

Figure 24: Continued.

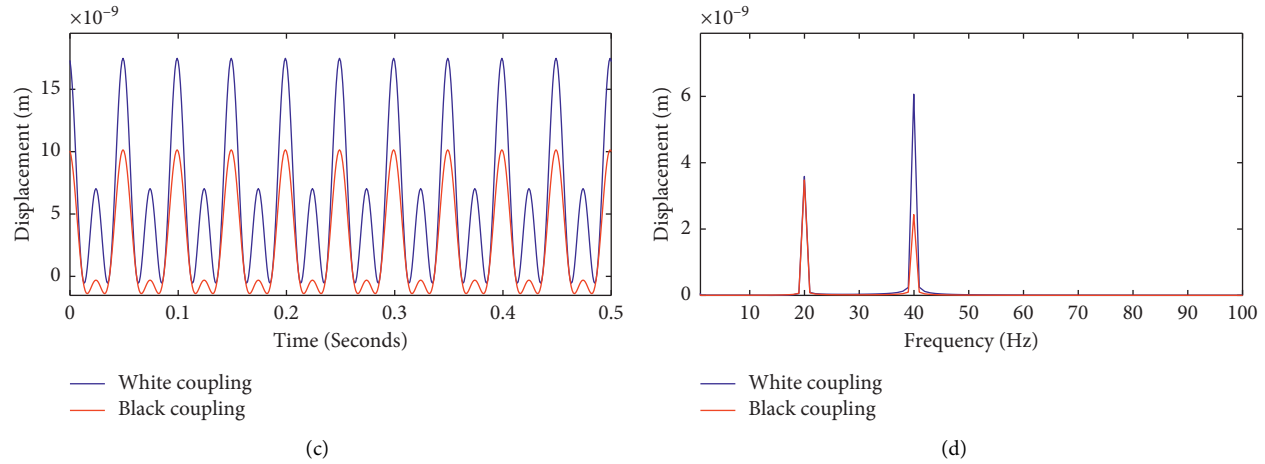

FIGURE 24: Effects of changing the coupling type in the y direction for a system with imbalance and parallel misalignment. (a) Time response of y1. (b) Frequency response of y1. (c) Time response of y2. (d) Frequency response of y2.

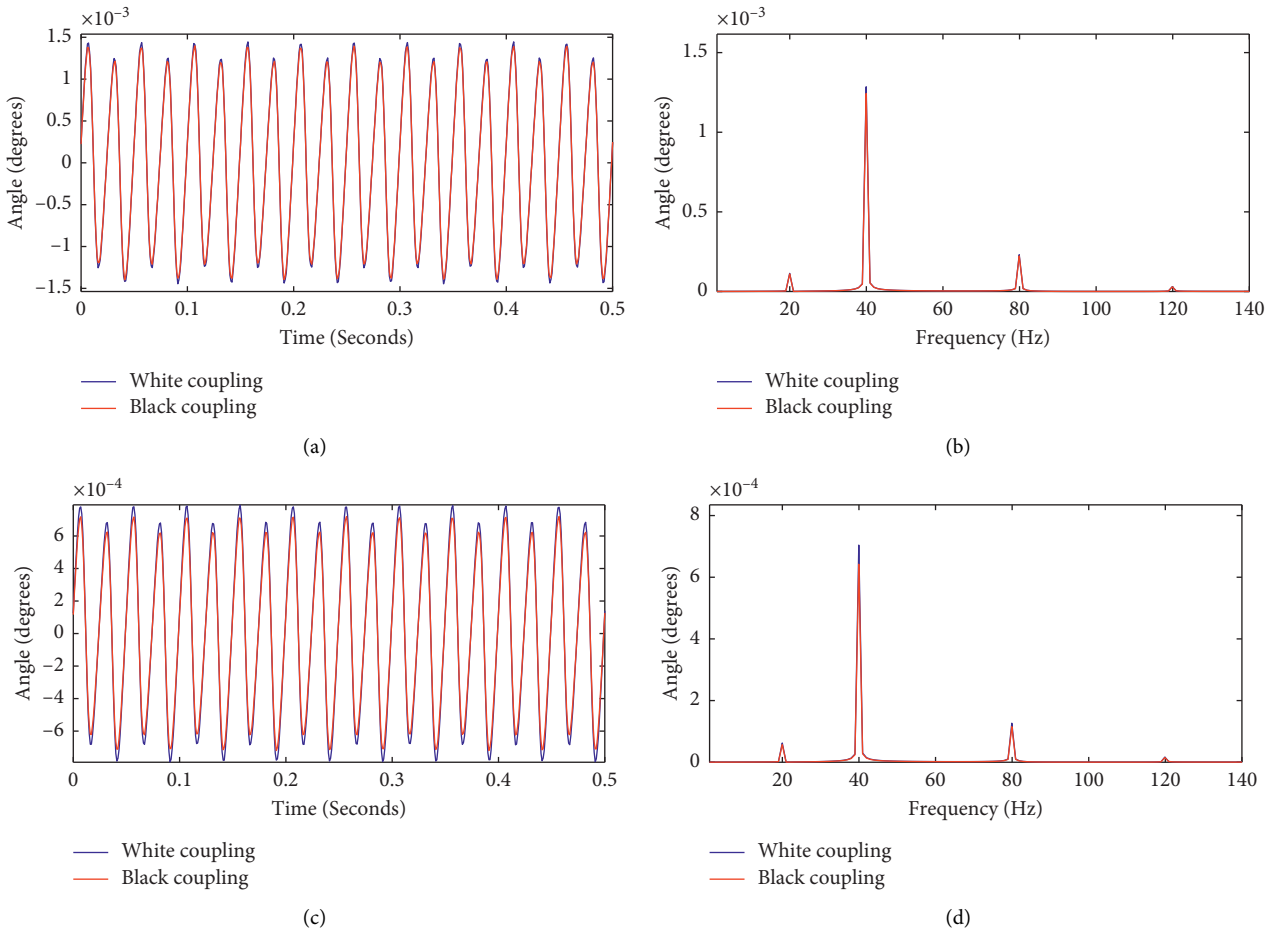

FIGURE 25: Effects of changing the coupling type in the θ direction for a system with imbalance and angular misalignment. (a) Time response of θ_1. (b) Frequency response of θ_1. (c) Time response of θ_2. (d) Frequency response of θ_2.

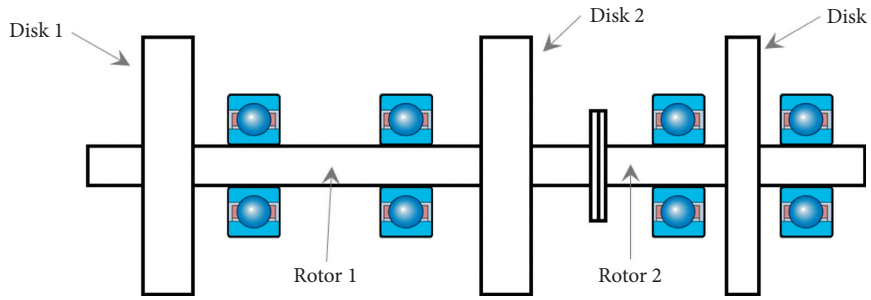

Figure 26: Wang and Gong's model [25].

Table 10: Data of the numerical model of Wang and Gong [25].

Rotor 1		
Diameter (mm)	Length (mm)	Mass (kg)
30	880	24.8
Rotor 2		
Diameter (m)	Length (mm)	Mass (kg)
40	400	5.92
Disks		
I_{z1} (kg/m^2)	I_{x1} (kg/m^2)	I_{y1} (kg/m^2)
0.05	0.025	0.025
Material properties of the rotor and disks		
Young's modulus (N/m^2)	Poisson's ratio	Density (kg/m^3)
$2.1E+11$	0.3	7800

rotor-coupling-bearing system's dynamic behavior in the presence of parallel and angular misalignments.

3.6.1. Effects of Altering Rotational Speed in the Presence of Imbalance and Parallel Misalignment. In the established rotor-coupling-bearing system with a constant parallel misalignment fault of 1 mm, the rotational speed was changed from 1200 rpm to 2700 rpm in steps of 300 rpm. The results are shown in Figure 21.

As portrayed in Figure 19, the response in the radial directions (x_1, y_1, x_2, y_2) at 1X increased significantly with increased rotational speed. This was mostly caused by the unbalanced force that acted on the system (Section 3.2). Furthermore, the increase in the 1X response was more rapid at Node 1 (x_1 and y_1) than at Node 2 (x_2 and y_2). This is probably because at Node 1, the system was more flexible than it was at Node 2. Moreover, the amplitude of 2X was constant despite the change in rotational speed. This was expected because the model of parallel misalignment force depends on the system's stiffness rather than rotational speed.

3.6.2. Effect of Altering the Rotational Speed in the Presence of Imbalance and Angular Misalignment. The effects of changing the rotational speed from 1200 rpm to 2700 rpm in steps of 300 rpm on a rotor-coupling-bearing system with both imbalance and angular misalignment faults were examined. Angular misalignment of 1° was maintained throughout the process. The results are shown in Figure 22.

Figure 22 shows that all peaks for 1X and its harmonics are sensitive to speed variation but to different degrees. In particular, the 2X and 4X amplitudes were found to be the most responsive to changes in speed variation, and they were more sensitive at Node 1(θ_1) than at Node 2(θ_2). This can be explained by the system being more flexible at Node 1 than at Node 2.

3.7. Effects of Changing the Coupling Type. The effects of changing the flexible coupling type were investigated for systems with parallel and angular misalignments.

3.7.1. Effects of Coupling Type on a System with Imbalance and Parallel Misalignment. The effects of changing the coupling type on the model response for combined imbalance and parallel misalignment of 1 mm were examined at a rotational speed of 1200 rpm. The results in the radial directions x_1 and x_2 are shown in Figure 23, and the results in the radial directions y_1 and y_2 are shown in Figure 24.

Based on the time response graphs, one can see that the amplitudes were higher for the white coupling, which was stiffer and was therefore unable to accommodate the deformations as in the case of the black one. In the frequency domain, the peaks located at 1X did not show a perceptible variation (a difference of only 2.4%). However, for the peaks located at 2X, the amplitudes for white coupling were 60% higher because of the difference in the stiffness.

3.7.2. Effects of Coupling Type on a System with Imbalance and Angular Misalignment. The effects of swapping the white coupling for the black one were analyzed for a system with imbalance and 1° of angular misalignment, at a

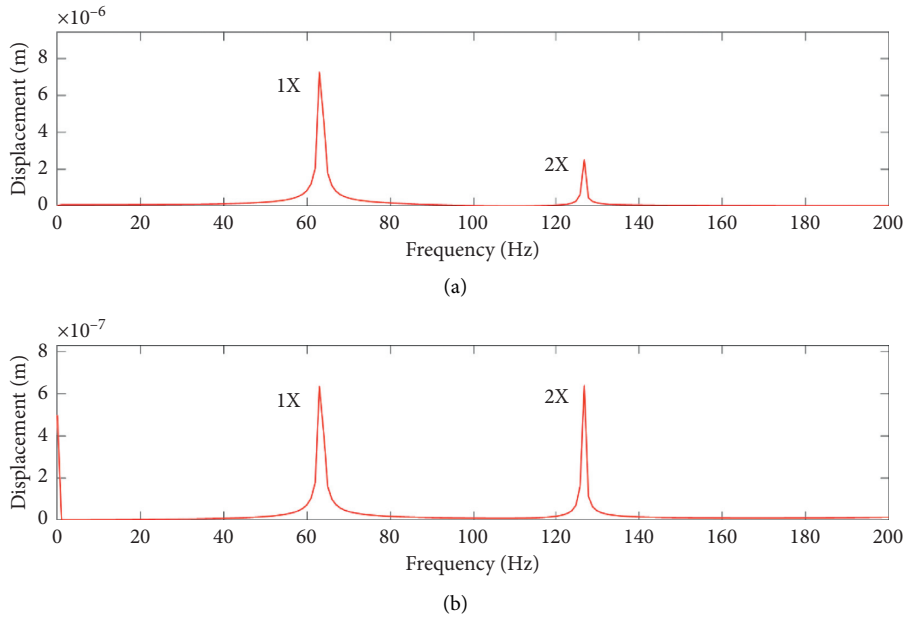

Figure 27: Response to the effects of imbalance and parallel misalignment based on Wang and Gong's parameters. (a) Frequency response of x1. (b) Frequency response of x2.

Table 11: Comparison of our model versus that of Wang and Gong [25].

Model		Amplitudes (μm)	
		Horizontal direction	Vertical direction
@1 × rpm	Current Model	7.25	0.63
	Wang and Gong	6.66	0.92
@2 × rpm	Current Model	2.51	0.64
	Wang and Gong	2.22	0.33

rotational speed of 1200 rpm. Figure 25 presents the simulation results for this particular case.

Figure 25 shows that changing the coupling type did not produce a noticeable difference in the vibration spectrum recorded in the θ direction. We expected the black coupling to absorb more vibrations, which would result in reduced amplitudes. However, the moments of inertia in the two couplings were small, and the difference between them was only minor, meaning that no effect of changing the coupling could be seen.

3.8. Validation of the Numerical Model. To verify our proposed model, the simulation presented here was compared with a similar study by Wang and Gong [25] that provided a numerical simulation of a system that included parallel misalignment. This particular model was chosen because the authors provided enough data to allow a comparison of the two models. Wang and Gong simulated the vertical and horizontal displacement response at the coupling location. Some of the parameters had to be assumed, as the authors had not supplied them, and we drew on our prior expertise to make these assumptions. Figure 26 illustrates the simulated model of Wang and Gong [25].

Before we can compare the models, we needed to clarify several assumptions so we could implement the model with the available data. Each system was divided into two subsystems (with a specific mass, stiffness, and damping values) and analyzed with 12 DOF, as was the case for our model. The stiffness in the axial direction was assumed to be 10 times higher than the bending stiffness; the angular stiffness was assumed to be 1/1000 of the radial stiffness. These were the ratios obtained here for a flexible coupling (Section 2.3). Table 10 presents the data provided by Wang and Gong.

Wang and Gong [25] provided data on the vertical and horizontal radial vibrations of the rotating system at Node 1. Their system was tested with 1 mm of parallel misalignment at a rotation speed of 3800 rpm. We used our model with the parameters provided by Wang and Gong to obtain the response, displayed in Figure 27, in the time and frequency domains.

Similarly, for both studies, the amplitudes in the horizontal direction were higher than those in the vertical direction. This aligned with our expectations because the bearings were fixed to the ground, preventing vertical movement. Table 11 compares the amplitudes of our model against that of Wang and Gong.

The two sets of results agree fairly close to each other. The minor differences may well have arisen from the assumptions about the mass, damping, and stiffness parameter, which were not provided by Wang and Gong.

4. Conclusion

In this paper, a model was developed to investigate the dynamic behaviors and vibration characteristics of a rotating system with imbalance and misalignment faults in the coupling. The simulated system consisted of an assembly of two shafts interconnected by a flexible coupling. In total, the system's motion is described by a set of 12 DOF. The vibration characteristics in the radial (horizontal and vertical) and angular direction were revealed by numerical analysis by using Matlab and Simulink, giving rise to several conclusions:

(i) The effect of pure imbalance made the system oscillate in a harmonic way that manifested as a pure sine wave in the time domain and a single peak in the frequency domain. However, the combined effects of imbalance and misalignment produced a nonharmonic response. Besides the fundamental frequency components of the rotating assembly (1X), one can see the existence of new components, with frequencies that were multiples of the fundamental one (2X and 4X).

(ii) In the simulation of the coupled effect of imbalance and parallel misalignment, the following could be observed:

  (1) Varying the parallel misalignment had practically no influence on the amplitudes of the 1X peaks in all radial directions
  (2) The amplitudes of the 2X peaks were found to increase linearly with an increase in the parallel misalignment

(iii) In the simulation of the combined effect of imbalance and angular misalignment faults, the following could be observed:

  (1) The impact on the amplitude of the second harmonic of speed (2X) of adding 1° of misalignment was significant
  (2) Remarkable peaks at 1X, 2X, and 4X can be observed in the vibration spectra, with the 2X component being the strongest

(iv) In the simulation of the effect of varying the angular misalignment, the following could be observed:

  (1) Varying the angular misalignment had almost no effect on the 1X amplitudes
  (2) The amplitudes of 2X and 4X increased with an increase in the angular misalignment
  (3) In particular, the 2X component was the most sensitive, which confirms the findings of previous researchers and practitioners

(v) In a simulation of the effect of rotational speed, the following could be observed:

  (1) For a system with imbalance and parallel misalignment, the response amplitudes in the radial directions at 1X significantly increased with faster rotational speeds.
  (2) For a system with imbalance and angular misalignment, all peaks for 1X and its harmonics were sensitive to speed variations but to different degrees. In particular, the 2X and 4X amplitudes were found to be the most responsive to speed variation.

Data Availability

The underlying data supporting the results of this study can be shared anytime via Dropbox or Google Drive.

Conflicts of Interest

The authors declare that they have no conflicts of interest.

Acknowledgments

The authors gratefully acknowledge the financial support provided by the Qatar National Research Fund through the National Priorities Research Program under grant number NPRP 11S-1220-170112 and Qatar University Internal Grant QUCG-CENG-19/20-6.

References

[1] B. Klebanov, D. Barlam, and F. Nystrom, *Machine Elements: Life and Design*, CRC Press, New York, NY, USA, 1st edition, 2007.

[2] A. Muszynska, *Rotordynamics*, CRC Press, New York, NY, USA, 1st edition, 2005.

[3] J. Piotrowski, *Shaft Alignment Handbook*, CRC Press, New York, NY, USA, 3rd edition, 2006.

[4] D. P. Hujare and M. G. Karnik, "Vibration responses of parallel misalignment in Al shaft rotor bearing system with rigid coupling," *Materials Today: Proceedings*, vol. 5, no. 11, pp. 23863–23871, 2018.

[5] K. Elbhbah and J. K. Sinha, "Vibration-based condition monitoring of rotating machines using a machine composite spectrum," *Journal of Sound and Vibration*, vol. 332, no. 11, pp. 2831–2845, 2013.

[6] M. Adams Jr., *Rotating Machinery Vibration: From Analysis to Troubleshooting*, CRC Press, New York, NY, USA, 2nd edition, 2010.

[7] J. Vance, F. Zeidan, and B. Murphy, *Machinery Vibration and Rotor Dynamics*, John Wiley & Sons, New Jersey, NJ, USA, 1st edition, 2010.

[8] G. N. D. S. Sudhakar and A. S. Sekhar, "Coupling misalignment in rotating machines: modelling, effects and monitoring," *Noise & Vibration Worldwide*, vol. 40, no. 1, pp. 17–39, 2009.

[9] C. B. Gibbons, "Coupling misalignment forces," *Texas A&M University*, vol. 40, pp. 111–116, 1976.

[10] M. Xu and R. D. Marangoni, "Vibration analysis of A motor-flexible coupling-rotor system subject to misalignment and unbalance, Part II: experimental validation," *Journal of Sound and Vibration*, vol. 176, no. 5, pp. 681–691, 1994.

[11] A. S. Sekhar and B. S. Prabhu, "Effects of coupling misalignment on vibrations of rotating machinery," *Journal of Sound and Vibration*, vol. 185, no. 4, pp. 655–671, 1995.
[12] M. Xu and R. D. Marangoni, "Vibration analysis of A motor-flexible coupling-rotor system subject to misalignment and unbalance, Part I: theoretical model and analysis," *Journal of Sound and Vibration*, vol. 176, no. 5, pp. 663–679, 1994.
[13] D. L. Dewell and L. D. Mitchell, "Detection of a misaligned disk coupling using spectrum analysis," *Journal of Vibration and Acoustics*, vol. 106, no. 1, pp. 9–16, 1984.
[14] P. Pennacchi, A. Vania, and S. Chatterton, "Nonlinear effects caused by coupling misalignment in rotors equipped with journal bearings," *Mechanical Systems and Signal Processing*, vol. 30, pp. 306–322, 2012.
[15] K. M. Al-Hussain and I. Redmond, "Dynamic response of two rotors connected by rigid mechanical coupling with parallel misalignment," *Journal of Sound and Vibration*, vol. 249, no. 3, pp. 483–498, 2002.
[16] I. Redmond, "Shaft misalignment and vibration: a model," *Saudi Aramco Journal of Technology*, vol. 40, pp. 41–51, 2007.
[17] A. W. Lees, "Misalignment in rigidly coupled rotors," *Journal of Sound and Vibration*, vol. 305, no. 1-2, pp. 261–271, 2007.
[18] A. K. Jalan and A. R. Mohanty, "Model based fault diagnosis of a rotor-bearing system for misalignment and unbalance under steady-state condition," *Journal of Sound and Vibration*, vol. 327, no. 3–5, pp. 604–622, 2009.
[19] V. Hariharan and P. S. S. Srinivasan, "Vibration analysis of misaligned shaft–ball bearing system," *Songklanakarin Journal of Science and Technology*, vol. 33, no. 1, pp. 61–68, 2011.
[20] V. Hariharan and P. S. S. Srinivasan, "Vibration analysis of misaligned shaft -ball bearing system," *Indian Journal of Science and Technology*, vol. 2, no. 9, pp. 45–50, 2009.
[21] T. H. Patel and A. K. Darpe, "Vibration response of misaligned rotors," *Journal of Sound and Vibration*, vol. 325, no. 3, pp. 609–628, 2009.
[22] J.-L. Lin, J. Y.-C. Liu, C.-W. Li, L.-F. Tsai, and H.-Y. Chung, "Motor shaft misalignment detection using multiscale entropy with wavelet denoising," *Expert Systems with Applications*, vol. 37, no. 10, pp. 7200–7204, 2010.
[23] Z. Li, J. Li, and M. Li, "Nonlinear dynamics of unsymmetrical rotor-bearing system with fault of parallel misalignment," *Advances in Mechanical Engineering*, vol. 10, no. 5, pp. 1–17, 2018.
[24] N. Wang and D. Jiang, "Vibration response characteristics of a dual-rotor with unbalance-misalignment coupling faults: theoretical analysis and experimental study," *Mechanism and Machine Theory*, vol. 125, pp. 207–219, 2018.
[25] H. Wang and J. Gong, "Dynamic analysis of coupling misalignment and unbalance coupled faults," *Journal of Low Frequency Noise, Vibration and Active Control*, vol. 38, no. 2, pp. 363–376, 2019.
[26] R. S. Srinivas, R. Tiwari, and C. Kannababu, "Model based analysis and identification of multiple fault parameters in coupled rotor systems with offset discs in the presence of angular misalignment and integrated with an active magnetic bearing," *Journal of Sound and Vibration*, vol. 450, pp. 109–140, 2019.
[27] N. Sawalhi, S. Ganeriwala, and M. Tóth, "Parallel misalignment modeling and coupling bending stiffness measurement of a rotor-bearing system," *Applied Acoustics*, vol. 144, pp. 124–141, 2019.
[28] Y. Xia, J. Pang, L. Yang, Q. Zhao, and X. Yang, "Study on vibration response and orbits of misaligned rigid rotors connected by hexangular flexible coupling," *Applied Acoustics*, vol. 155, pp. 286–296, 2019.
[29] Ruland Manufacturing Co., *Flexible Beam Couplings from RULAND*, Technical Catalog, London, UK, 2020.
[30] B. Badri, "Comportement vibratoire de rotors opérant à hautes vitesses et détection des défauts de roulements," 2014.